REPORT DOCUMENTATION PAGE

Form Approved OMB NO. 0704-0188

1. REPORT DATE (DD-MM-YYYY)	2. REPORT TYPE	3. DATES COVERED (From - To)
19-10-2021	Final Report	1-Dec-2017 - 30-Mar-2021

4. TITLE AND SUBTITLE
Final Report: Understanding Nonlinear Coherent Structure Interactions in Boundary-Layer Transition using Adaptive Signal Analysis

5a. CONTRACT NUMBER
W911NF-18-1-0030

5b. GRANT NUMBER

5c. PROGRAM ELEMENT NUMBER
611102

6. AUTHORS

5d. PROJECT NUMBER

5e. TASK NUMBER

5f. WORK UNIT NUMBER

7. PERFORMING ORGANIZATION NAMES AND ADDRESSES
University of Illinois - Urbana - Champaign
c/o Office of Sponsored Programs
1901 S. First Street, Suite A
Champaign, IL 61820 -7406

8. PERFORMING ORGANIZATION REPORT NUMBER

9. SPONSORING/MONITORING AGENCY NAME(S) AND ADDRESS (ES)
U.S. Army Research Office
P.O. Box 12211
Research Triangle Park, NC 27709-2211

10. SPONSOR/MONITOR'S ACRONYM(S)
ARO

11. SPONSOR/MONITOR'S REPORT NUMBER(S)
69650-EG-YIP.3

12. DISTRIBUTION AVAILIBILITY STATEMENT
Approved for public release; distribution is unlimited.

13. SUPPLEMENTARY NOTES
The views, opinions and/or findings contained in this report are those of the author(s) and should not contrued as an official Department of the Army position, policy or decision, unless so designated by other documentation.

14. ABSTRACT

15. SUBJECT TERMS

16. SECURITY CLASSIFICATION OF:			17. LIMITATION OF ABSTRACT	15. NUMBER OF PAGES	19a. NAME OF RESPONSIBLE PERSON
a. REPORT	b. ABSTRACT	c. THIS PAGE			Phillip Ansell
UU	UU	UU	UU		19b. TELEPHONE NUMBER 217-300-0949

RPPR Final Report
as of 19-Oct-2021

Agency Code: 21XD

Proposal Number: 69650EGYIP **Agreement Number: W911NF-18-1-0030**
INVESTIGATOR(S):

Name: Phillip Ansell
Email: ansell1@illinois.edu
Phone Number: 2173000949
Principal: Y

Organization: **University of Illinois - Urbana - Champaign (UIUC)**
Address: c/o Office of Sponsored Programs, Champaign, IL 618207406
Country: USA
DUNS Number: 041544081 EIN: 376000511
Report Date: 30-Jun-2021 Date Received: 19-Oct-2021
Final Report for Period Beginning 01-Dec-2017 and Ending 30-Mar-2021
Title: Understanding Nonlinear Coherent Structure Interactions in Boundary-Layer Transition using Adaptive Signal Analysis
Begin Performance Period: 01-Dec-2017 **End Performance Period:** 30-Mar-2021
Report Term: 0-Other
Submitted By: Phillip Ansell Email: ansell1@illinois.edu
Phone: (217) 300-0949
Distribution Statement: 1-Approved for public release; distribution is unlimited.

STEM Degrees: 2 **STEM Participants:**

Major Goals: The high-level objectives of the research program included:
- Develop a multivariate, multi-dimensional empirical mode decomposition processing method capable of performing scale separation of three-dimensional, three-component velocity fields.
- Extract multi-scale contributions of turbulent fluctuations in a transitional boundary layer using adaptive modal decomposition
- Determine amplitude, phase, and frequency/wavenumber evolution of unsteady modes throughout transition and relate to physical characteristics of nonlinear breakdown to turbulent flow

Accomplishments: All major goals were accomplished through the current study. New methods for modal decomposition and analysis of fluid flows were produced. Application of these methods to canonical cases of boundary layer transition have revealed an improved understanding of:
- The growth and bifurcations of instabilities leading up to the breakdown to turbulent flow
- The abrupt emergence of broad-band turbulent spectral content, and initial persistence of initial instability modes into the early turbulent boundary layer
- Anticipated sources of skin friction overshoot produced at the completion of natural boundary-layer transition

It should be noted that an initial hypothesis configured for the program included a study of the space-wavenumber evolution of primary instabilities, and how these modes feed into the broad-band turbulence spectrum. After completing this study, it appears as though there is not perceptively-direct link between these flow components.

Training Opportunities: Supported one MS student (graduated) and two PhD students (one of two currently graduated, other pending)

Results Dissemination: Thirumalaisamy, Mruthun R., and Phillip J. Ansell. "Fast and adaptive empirical mode decomposition for multidimensional, multivariate signals." IEEE Signal Processing Letters 25.10 (2018): 1550-1554.

Cheng, Shyuan, Leonardo P. Chamorro, and Phillip J. Ansell. "On the H-type transition to turbulence—Laboratory experiments and reduced-order modeling." Physics of Fluids 33.2 (2021): 024105.

Gupta, Rohit, et al. "Unsteady spectra of velocity field for a canonical dynamic stall process." APS Division of Fluid Dynamics Meeting Abstracts. 2019.

RPPR Final Report
as of 19-Oct-2021

Honors and Awards: University of Illinois at Urbana-Champaign, Grainger College of Engineering: Dean's Award for Excellence in Research (2019)

University of Illinois at Urbana-Champaign, Department of Aerospace Engineering: Allen Ormsbee Faculty Fellow (2019)

AIAA (University of Illinois Undergraduate Student Chapter) Teacher of the Year (2020)

Penn State Engineering Alumni Society: Young Alumni Achievement Award (2021)

Protocol Activity Status:

Technology Transfer: Nothing to Report

PARTICIPANTS:

Participant Type: PD/PI
Participant: Phillip John Ansell
Person Months Worked: 1.00 **Funding Support:**
Project Contribution:
National Academy Member: N

Participant Type: Co-Investigator
Participant: Leonardo Chammorro
Person Months Worked: 1.00 **Funding Support:**
Project Contribution:
National Academy Member: N

Participant Type: Graduate Student (research assistant)
Participant: Mruthun Thirumalaisamy
Person Months Worked: 9.00 **Funding Support:**
Project Contribution:
National Academy Member: N

Participant Type: Graduate Student (research assistant)
Participant: Jeffrey Cheng
Person Months Worked: 9.00 **Funding Support:**
Project Contribution:
National Academy Member: N

Participant Type: Graduate Student (research assistant)
Participant: Rohit Gupta
Person Months Worked: 9.00 **Funding Support:**
Project Contribution:
National Academy Member: N

RPPR Final Report
as of 19-Oct-2021

ARTICLES:

Publication Type: Journal Article Peer Reviewed: Y **Publication Status:** 1-Published
Journal: IEEE Signal Processing Letters
Publication Identifier Type: DOI Publication Identifier: 10.1109/LSP.2018.2867335
Volume: 25 Issue: 10 First Page #: 1550
Date Submitted: 9/18/18 12:00AM Date Published: 10/1/18 5:00AM
Publication Location:
Article Title: Fast and Adaptive Empirical Mode Decomposition for Multidimensional, Multivariate Signals
Authors: Mruthun R. Thirumalaisamy, Phillip J. Ansell
Keywords: Empirical mode decomposition (EMD), FA-EMD, modal analysis, multidimensional EMD, multivariate signal.
Abstract: Over the last decade, empirical mode decomposition (EMD) has developed into a versatile tool for adaptive, scale-based modal decomposition. EMD has proven to be capable of decomposing multivariate signals with cross-channel mode alignment. However, the algorithms for envelope identification in multivariate EMD come with a computational burden rendering it unsuitable for the large computational demands of multidimensional signal processing. The current work introduces an alternative approach to multivariate EMD, and by combining it with existing fast and adaptive algorithms, paves the way for performing multivariate EMD on multidimensional signals.
Distribution Statement: 3-Distribution authorized to U.S. Government Agencies and their contractors
Acknowledged Federal Support: **Y**

Publication Type: Journal Article Peer Reviewed: Y **Publication Status:** 1-Published
Journal: Physics of Fluids
Publication Identifier Type: DOI Publication Identifier: 10.1063/5.0036082
Volume: 33 Issue: First Page #:
Date Submitted: Date Published: 2/19/21 6:00AM
Publication Location:
Article Title: On the H-type transition to turbulence—Laboratory experiments and reduced-order modeling
Authors: Shyuan Cheng, Leonardo Chammorro, Phillip Ansell
Keywords: transition, refractive index match, particle image velocimetry, proper orthogonal decomposition, reduced-order modeling
Abstract: A series of experiments were conducted to understand the sources of local, high-amplitude velocity fluctuations produced at the late stages of boundary-layer flow transition to turbulence. The laboratory experiments considered the controlled injection of Tollmien–Schlichting (TS) waves into a nearly zero pressure gradient, laminar boundary layer, resulting in H-type transition to turbulence. Proper orthogonal decomposition (POD) was used to extract the energetic coherent structures within the transitional flow field obtained with particle image velocimetry. The lower portion of the large-scale hairpin vortex structure was observed to be primarily responsible for the overshoot mechanisms, which was well captured in a reduced-order model of the velocity field. The first four POD modes were used to create this reduced-order model, which, while only consisting of ?15% of the total turbulence kinetic energy of the original velocity field, was able to capture ?85% of the peak Reynolds stress
Distribution Statement: 1-Approved for public release; distribution is unlimited.
Acknowledged Federal Support: **Y**

RPPR Final Report
as of 19-Oct-2021

Partners

,

I certify that the information in the report is complete and accurate:
Signature: Phillip Ansell
Signature Date: 10/19/21 3:21AM

Understanding Nonlinear Coherent Structure Interactions in Boundary-Layer Transition using Adaptive Signal Analysis

Agreement # W911NF-18-1-0030

Final Report
(December 1, 2017 to March 30, 2021)

Principal Investigator:
Phillip J. Ansell
Department of Aerospace Engineering
University of Illinois at Urbana-Champaign
306 Talbot Laboratory, MC-236
104 South Wright Street
Urbana, Illinois 61801
ansell1@illinois.edu
(217) 300-0949

Abstract

In an effort to understand the fundamental source and sustainment mechanisms of a turbulent boundary layer, the evolution of energy spectra within a transitional boundary layer are studied. To conduct this program, an adaptive modal decomposition technique, the multi-variate, multidimensional empirical mode decomposition, was developed. This approach permitted velocity fields of interest to be separated into modal components as defined by an adaptive, empirical basis. In addition to this method, a Riesz transform and log-Gabor filter method were introduced to isolate key flow scales of interest and characterize wavenumber component projections of multi-dimensional velocity fields. Experimental data of controlled H-type transition were acquired in a refractive index matched flume, and a POD analysis was conducted to obtain an initial understanding of the energetic flow structures associated with the transition process. However, the majority of the current study utilized a direct numerical simulation dataset of K-type boundary-layer transition. When applying scale separation and spectral analysis techniques to these transitional flow data, the importance of large-scale features was commonly observed as a dominant contributor to the growth of unsteadiness leading to the emergence of turbulence. In this way, the separated large-scale features of the flow were observed to reach a relative maximum in amplitude immediately prior to breakdown of the secondary instability, leading to the emergence of a turbulent boundary layer. Further detailed analysis of spectrograms, showing the spanwise-wavenumber spectra of the streamwise velocity component, revealed a rapid excitation process of harmonics of the oblique mode. Shortly following this excitation process, a sudden emergence of distributed energy across a broad-band range of scales was observed. The narrow-band peaks associated with the oblique mode and associated harmonics were observed to persist following the emergence of the distributed turbulent flow scales, but decreased in amplitude with increasing streamwise distance. These observations suggest that the initial flow scales associated with the TS wave, oblique mode, and associated harmonics are not principally responsible for populating the turbulence spectrum at the conclusion of the transition event. While, naturally, these flow scales constitute the physical processes that lead to initially-local breakdown of the flow, these scales are not observed as clearly dispersing into the broad-band range of scales that constitutes the turbulent flow.

Objectives

The high-level objectives of the research program included:

- Develop a multivariate, multi-dimensional empirical mode decomposition processing method capable of performing scale separation of three-dimensional, three-component velocity fields.
- Extract multi-scale contributions of turbulent fluctuations in a transitional boundary layer using adaptive modal decomposition
- Determine amplitude, phase, and frequency/wavenumber evolution of unsteady modes throughout transition and relate to physical characteristics of nonlinear breakdown to turbulent flow

These objectives were approached using a novel modal decomposition method capable of classifying temporally- and/or spatially-dependent variations in energy content, without guaranteed periodicity or stationarity, across the velocity field of a transitional boundary layer.

Data Acquisition and Utilization

Throughout the current study, computational velocity field data of a natural boundary-layer transition process are utilized, alongside experimentally-acquired PIV data. While volumetric, time-resolved particle image velocimetry (PIV) data were intended to be utilized for the majority of the program, due to unforeseen challenges associated with configuring the experiments, only planar velocity field data were deemed of sufficient quality for analysis. As an alternative dataset, a set of computational direct numerical simulation data of a natural transition process were utilized. As an aside, since the experimental data did not capture the inner wall region of the boundary layer as intended, the computational data were actually deemed to be more appropriate for the research program. However, the experimental data did form a basis for a more conventional proper orthogonal decomposition (POD) analysis of the transitional velocity field, while the computational data were used for more detailed space-wavenumber modal analysis of the transitional flow physics.

Direct Numerical Simulation Data of H-Type Transition

The primary dataset used throughout the current study was a set of three-dimensional velocity field simulation results of an incompressible, K-Type transition, provided by Sayadi et al. [1]. These direct numerical simulation data were created as a means for studying the dynamics of turbulent boundary layers, making it ideal for the current program. These simulations were conducted on a zero pressure gradient flat plate, with a no-slip condition defined on the lower wall of the flow domain. The streamwise flow domain covered a range of Reynolds numbers of $1.0 \times 10^5 \leq \mathrm{Re}_x \leq 1.06 \times 10^6$ with a uniform freestream Mach number of $M_\infty = 0.2$. In these simulations, x_0 is defined as the streamwise position of the inlet, corresponding to the aforementioned Reynolds number of $\mathrm{Re}_x = 1.0 \times 10^5$. This length, however, is also used to define the spanwise and transverse domains of the velocity field. The transverse flow domain covered a region of $0 \leq y/x_0 \leq 0.92$ and the spanwise flow domain covered a region of $0 \leq z/x_0 \leq 0.6$. The computational domain used by these authors is shown in Fig. 1, after Sayadi et al.[1].

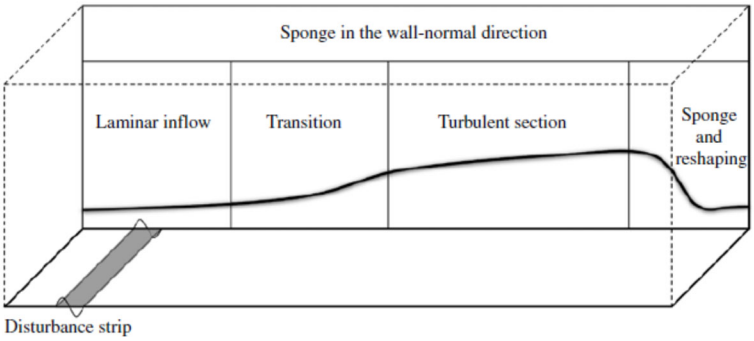

Fig. 1 Computational domain for K-Type transition DNS.

The wall-bounded flow across the inlet was defined as a canonical Blasius (laminar) boundary layer. The simulation is defined with a disturbance strip across the region defined as $1.36 \leq x/x_0 \leq 1.56$, having a blowing and suction boundary condition described by:

$$V(x,z,t) = A_1 f(x)\sin(\omega_1 t) + A_{1/2} f(x) g(z) \sin(\omega_{1/2} t) \quad (1)$$

where ω_1 and $\omega_{1/2}$ are the frequencies of the 2D TS wave and the oblique (spanwise) wave. This disturbance strip defined to seed the boundary-layer flow with a known Tollmien-Schlichting (TS) wave and secondary instability, such that the initial conditions of the transition process were well defined. The spanwise wavelength of the oblique mode was defined as $\lambda_0 = 0.15$, resulting in a spanwise flow domain of $4\lambda_0$ with periodic sidewall boundary conditions. Further information of the specific $f(x)$, $g(z)$ terms, amplitudes, and other settings can be found in Sayadi et al.[1]. However, the position of the selected frequency on the neutral stability curve is shown in Fig. 2 after these authors [1]. After growth of the primary TS wave instability, additional growth of the secondary instability takes place, leading to the development of well-defined Λ-vortex structures. The nonlinear breakdown of these coherent vortex structures then leads to the completion of the transition process and a subsequent turbulent boundary layer. An example profile of the streamwise velocity produced by this transitional flow case is shown in Fig. 3 after Sayadi et al.[1], represented by an xz-plane stationed away from the wall at position $y/\delta_{inlet} = 0.6$. For the analysis presented here, two periods of the primary instability mode are used to generate time-averaged results of the associated wavenumber content within the transitional velocity field.

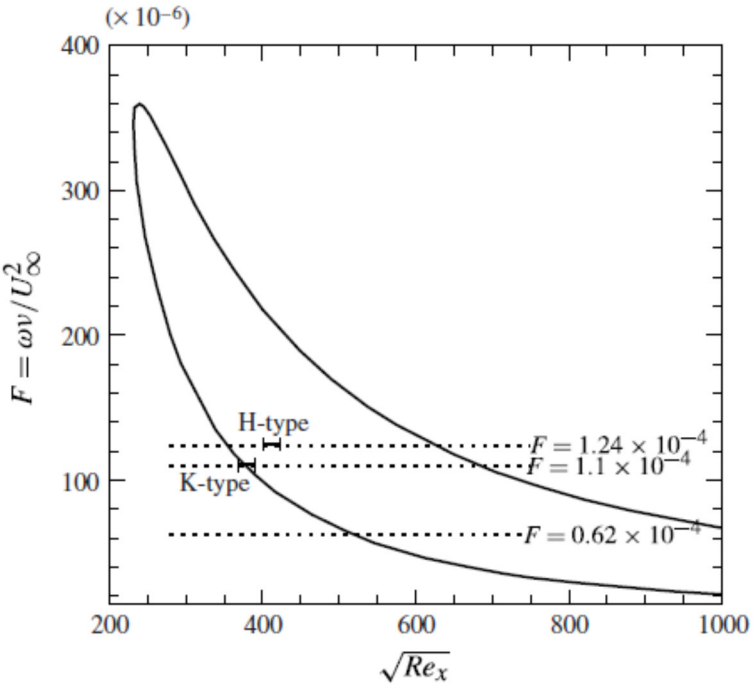

Fig. 2 Frequency selected for TS wave excitation, after Sayadi et al.[1]

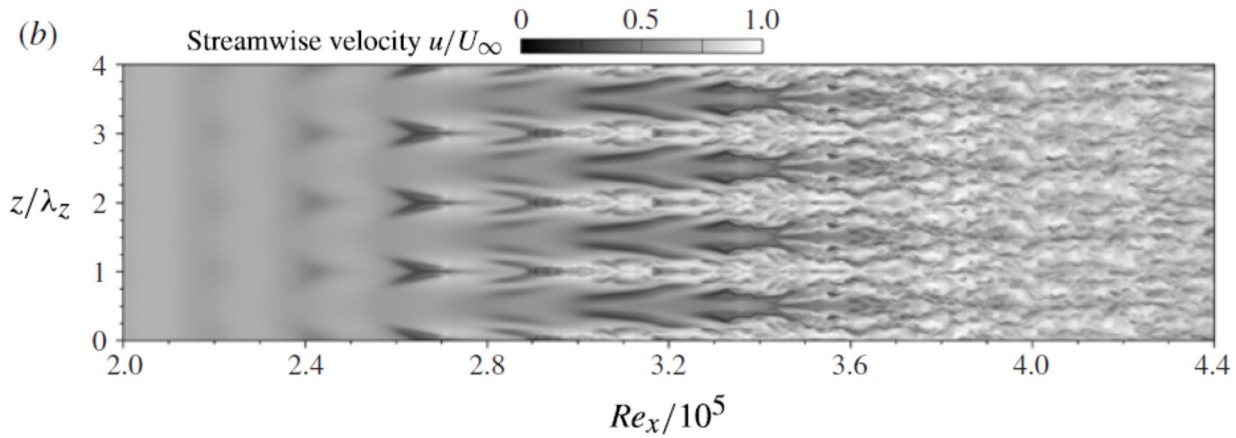

Fig. 3 Streamwise velocity across *xz*-plane at y/δ_{inlet} = 0.6, demonstrating transitional flow characteristics.

Particle Image Velocimetry Data Acquisition of H-Type Transition

The TS wave amplification and H-type transition process of a flat-plate boundary layer was experimentally studied in a 2.5-m long, 112.5-mm wide, and 112.5-mm high recirculating, refractive-index matching (RIM) channel located in the Renewable Energy and Turbulent Environment Laboratory at the University of Illinois, as shown in Fig. 4. The upstream channel duct has a contraction section with an area ratio of 4.375:1, which induces a flow with negligible turbulence intensity. The boundary-layer profile without external disturbance at $Re_x = 3 \times 10^5$ is given in Fig. 5, which is observed to follow a Blasius profile. Aqueous sodium iodide solution of ~63% by weight was used as the working fluid; its refractive index matched that of the flume walls, which significantly reduced the intensity of associated reflections in the vicinity of the wall surface. This aspect allowed for high accuracy velocity data to be resolved across the very-near wall locations in the PIV field of view (FOV). The fluid has a density of $\rho_0 = 1800$ kg/m^3 and a kinematic viscosity of $\nu = 1.1 \times 10^{-6}$ m^2/s. For additional details on the facility, see Blois et al.;[2] additional information on the refractive-index-matching technique can be found in Bai and Katz[3] and Hamed et al.[4]

A vibrating ribbon was used to induce Tollmien–Schlichting (TS) instability waves as a mechanism to trigger the laminar–turbulent transition process. This method has been widely used to produce TS waves since the original experimental verification of TS waves decades ago.[5] A 355 μm-thick copper ribbon was laminated by a layer of 25 μm Kapton tape on each side to insulate the electric current passing through the ribbon from the fluid; see a basic schematic of the setup in Fig. 4. A verification test showed that, without the supply of current, the stationary ribbon presence did not significantly influence the boundary-layer profile; Blasius profiles were obtained with and without the stationary ribbon (see Fig. 5) The ribbon periodic sinusoidal motion was induced by a Lorentz force. The ribbon forcing was created by passing an alternating current at a prescribed frequency through the ribbon, which interacted with two rows of permanent magnets mounting under the channel bottom wall. The current was produced from a function generator and amplified, allowing for controllable variation of the ribbon motion frequency and amplitude. For the experiments conducted in the current study, the circuit oscillation frequency was set to 1.6 Hz and the current output of 65.3 A. This resulted in a ~6

mm maximum peak-to-peak vibration amplitude at the ribbon center. Additional details on the vibrating ribbon technique can be found in Boiko et al.,[6] Gilev and Kozlov,[7] and Klebanoff et al.[8]

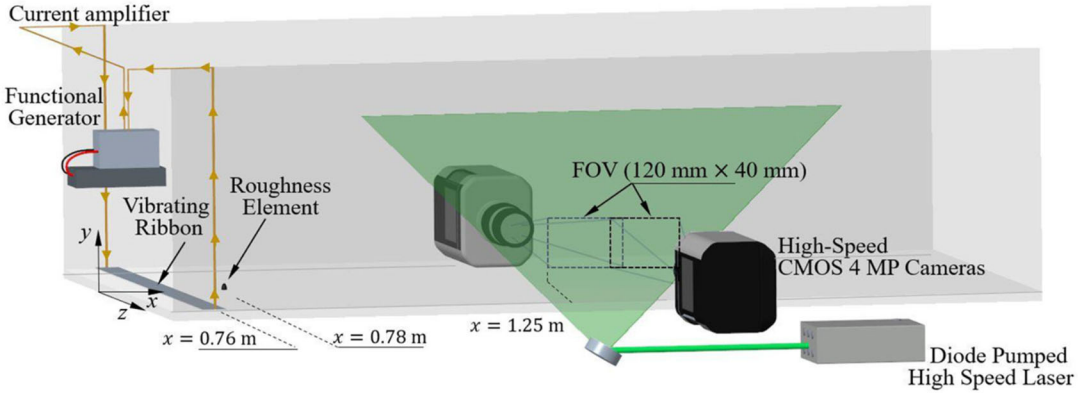

Fig. 4 TR-PIV experimental configuration in refractive-index matched flume.

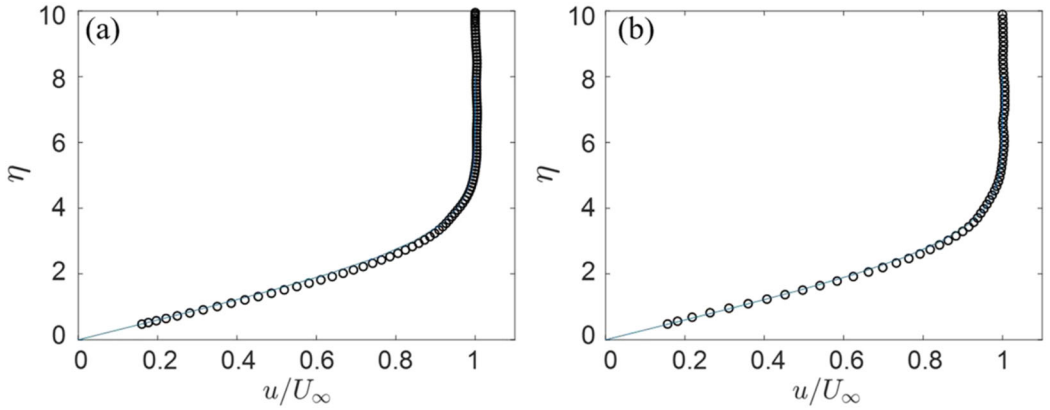

Fig. 5 Boundary layer velocity profile measured without (a) and with (b) unactuated ribbon installed in RIM flume; Blasius theoretical solution provided as solid curve

The ribbon periodic vibration was tracked with a customized particle tracking velocimetry (PTV) system using a Mikrotron EoSens 4CXP MC4082 high-speed camera at 4 MP resolution and a Nikon AF Micro-Nikkor lens of 50 mm focal length and a focal ratio of f/2.8. Fiducial marks were added every 15 mm along the ribbon top surface, which was illuminated with a Stanley Lithium–Ion Halogen Spotlight and tracked at 300 Hz over a 30 s sampling period. The trajectory of the ribbon at a given instant was obtained by linking the fiducial points using a piecewise polynomial interpolation. Fig. 6 demonstrates the ribbon vibration trajectory throughout the spanwise direction, with L = 0.1125 m serving as the width of the channel. Velocity fields of the flow transition process were acquired across a streamwise plane beginning 1.25 m downstream of the flume inlet using a high-speed planar PIV system from TSI. Two cameras were used to interrogate two 120 × 40 mm^2 field of views (FOVs) with a slight overlap. The FOVs were located at the center of the RIM flume, immediately above the bottom wall. The FOVs were illuminated with a 1 mm thick laser sheet generated by 50 mJ pulses from a high

speed, dual cavity Amplitude Terra PIV Nd:YLF laser. The working fluid was seeded with 14 μm, silver-coated hollow glass spheres. Three sets of 1000 image pairs (3000 vector fields) were collected at an acquisition frequency of 100 Hz, using a pair of 2560 × 1600 pixels CMOS Phantom M340 cameras with 12 GB on-board memory. The image pairs were interrogated using a recursive cross-correlation method via the TSI Insight 4G software. The final interrogation window had a size of 24 × 24 pixels with 50% overlap, resulting in a vector grid spacing $\Delta x = \Delta y = 420$ μm.

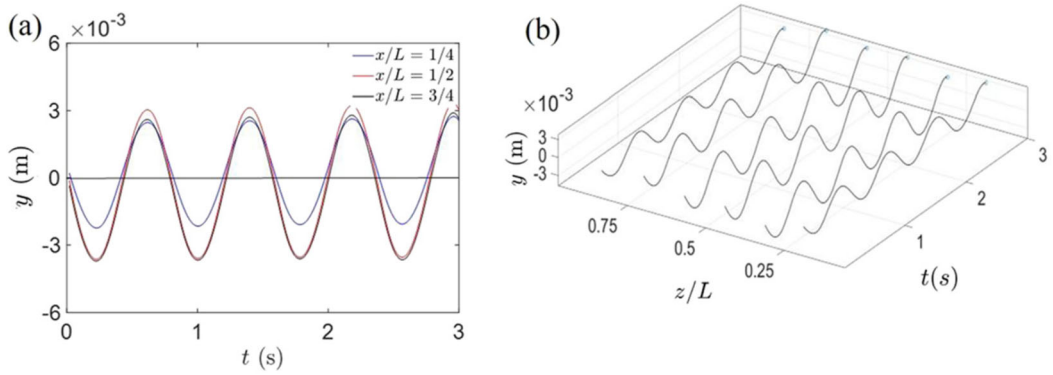

Fig. 6 Ribbon vibration amplitude, (a) 2D trajectory and, (3) 3D trajectory for selected locations.

Based on the location of the ribbon, the frequency of TS waves corresponding to a neutral stability condition were determined from linear stability theory, [9,10] as shown in Fig. 7. For the experiments conducted in the current study, the freestream velocity of the flume corresponded to $U_\infty = 0.175$ m/s, and the vibrating ribbon was placed $x = 0.76$ m downstream of the inlet. The working fluid was temperature-controlled such that constant density and viscosity were maintained, and a repeatable Reynolds number was achieved given a consistent freestream velocity and streamwise position. The excitation frequency and installation location of the vibrating ribbon corresponded to $F = 2\pi fv/U_\infty^2 = 1.8 \times 10^{-4}$ and $R = 1.72\sqrt{Re_x} = 598$. The position of this dimensionless frequency on the neutral stability curve of a Blasius boundary layer is shown in Fig. 7.

Linear stability theory also indicates that the TS wave excitation would occur at the resonance condition $\omega_1 = 2\omega_{1/2}$ for an H-type transition,[11,12] where ω_1 and $\omega_{1/2}$ are the frequencies of the two-dimensional TS and the oblique waves. This condition was obtained by placing a semi-elliptical roughness element with a diameter of $D = 4$ mm and a height of $h = 4.5$ mm at the flume center. The roughness element dimension was selected to have a $Re_h = U_{local}h/v = 520$, below the typical Reynolds number required for exciting bypass transition. Given the freestream velocity, the distance between the roughness element and the side walls (also acted as disturbance) was consistent with the wavenumber required to produce the associated $\omega_{1/2}$ condition for amplification for associated oblique waves of H-type transition, resulting in the generation of inherent spanwise sub-harmonics and a staggered pattern of coherent structures in the spanwise direction. This approach of introducing spanwise perturbations [13,14] allowed the location of secondary breakdown mechanisms to be more effectively controlled. The TS waves

were measured across the late stages of the transition process, where exponential growth and nonlinear breakdown of initial disturbances occurred. The selected interrogation window covered a spatial domain where the onset of hairpin vortices and secondary breakdown were visible. The coordinate system is defined such that x, y, and z denote the streamwise, wall-normal, and spanwise directions, with $x = 0$ located at the beginning of the FOV, i.e., at 1.25 m downstream of the inlet.

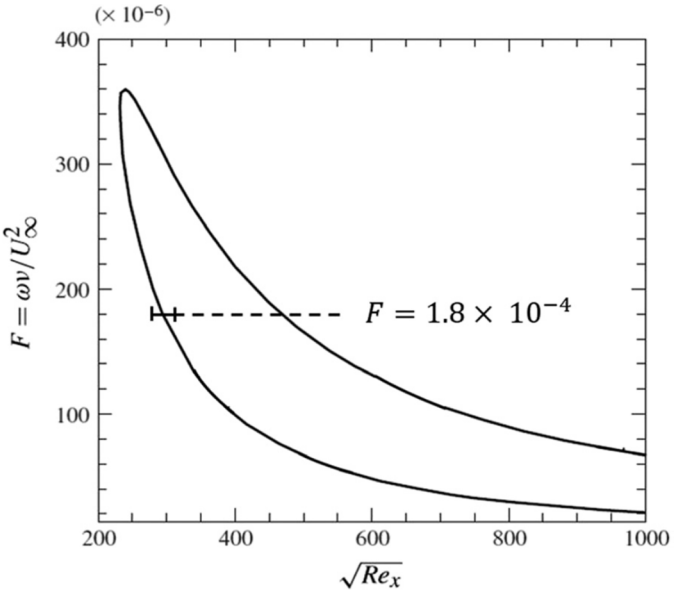

Fig. 7 Neutral stability curve with indicated frequency at Reynolds number of vibrating ribbon.

Data Processing Methods

Proper Orthogonal Decomposition

Proper orthogonal decomposition (POD) is a common modal analysis technique that is used to extract the dominant spatial features produced in a given flow field; it extracts modes that optimizes the mean square value of the flow field variable of interest by utilizing singular value decomposition (SVD).[15] This technique has proven to be extremely useful in studying the flow characteristics effected by coherent structures in transitional and spatially evolving flows.[16] For more information on POD and applications, see, e.g., Berkooz et al.[17] and Holmes et al.[18] In the current study, the snapshot POD as introduced by Sirovich[19] is chosen among various POD algorithms. Here, the 2D, two-component POD decomposes the stochastic velocity fluctuation matrix, $u'(x,y,t) = [u'v']^T$, into deterministic spatial-correlated patterns, $\varphi^n(x,y)$ (POD modes) [20] and their time-dependent coefficients $a^n(t)$, as follows:

$$u'(x,y,t) = \sum_{n=1}^{N} a^n(t)\phi^n(x,y) \tag{2}$$

where $N = 3000$ is the number of snapshots and u' is the velocity fluctuation vector matrix. Also, POD returns modes ranked by their energy content, E_n, after decomposing the velocity

fluctuations auto-covariance matrix. The energy content of a mode is obtained by dividing the eigenvalue of a particular mode by the sum of all N eigenvalues,[21] i.e., $E_n = \lambda_n \sum_{m=1}^{N} \lambda_m$, and can be interpreted as the single-mode contribution to the total turbulence kinetic energy. More information regarding implementation details of POD can be found in Meyer et al.[22] and Berkooz et al.[17]

Multivariate, Multi-Dimensional Empirical Mode Decomposition

In order to leverage the unique capabilities of adaptive modal decomposition for fluid flows, the empirical mode decomposition (EMD) algorithm is utilized. The original EMD method was developed in the late 1990's by Huang et al.[23] as a tool to extract modal components of a signal based on scale characteristics, with particular ability to appreciably handle nonstationary or intermittent content not well-suited for most decomposition techniques. Since the method does not assume a fixed basis for the decomposition process, it is also able to adaptively determine suitable functions to represent the original signal with very few modal components.

Since its original development, EMD has been utilized for a broad array of applications and technical domains. Various extensions of the basic EMD algorithm also exist. EMD has successfully been extended to incorporate multidimensional capabilities through a variety of methods [24-28]. On the other hand, the multivariate capabilities of EMD were outlined in [29-35]. However, these two techniques have so far been developed more or less independently from one another. For applications to real fluid flows, the ability to characterize modal content across multiple dimensions (e.g., x, y, and z) as a function of multiple vector components (e.g., u, v, and w) is a desired outcome. Seeing significant promise in such a capability, a multivariate, multi-dimensional EMD capability was thus developed as a component of the current study.

When applying EMD methods to datasets, one challenge is the relative computational expense of completing spline interpolation tasks when iteratively sifting the signal for modes. Given the broad range of scales present in many turbulent flows, the relative size of velocity datasets required to sufficiently resolve these ranges of scales can become quite large. As such, the utilization of a conventional spline interpolation method for sifting was deemed to be intractable for entire three-dimensional field data generated by computational simulations of fluid flows or experiments. As a consequence, a significant goal was also to develop the multivariate, multi-dimensional EMD approach to be computationally efficient, such that it could be applicable to large datasets.

Multidimensional EMD was first introduced in a primitive form by performing standard EMD on slices of multidimensional data. This method, however, suffers from the drawback of creating interslice discontinuities in the modes produced. An approach to reducing these discontinuities was introduced by the use of noise addition [36], but still did not solve the problem entirely. The most significant challenge of introducing a truly multidimensional EMD algorithm was overcoming the large computational cost requirements of sifting across expansive domains. The fast and adaptive extension to EMD has been shown to be capable of reducing the computational cost of processing multidimensional signals by several orders of magnitude [24]. The enabling

aspect of the method is that envelope generation is not carried out by expensive spline interpolation methods, but by the use of order statistics filters. The key parameter in the decomposition is the window size of the filtering process, which is what actually controls the characteristic scales of the modes that are extracted in a particular iteration of the EMD algorithm. The window size is determined as a function of the distance between extrema in the signal. In a sense, it is a measure of the size of the oscillatory scales present that can be extracted from the data to offer similar functionalities as spline-based extrema interpolation of traditional EMD methods.

In general, the three most important steps of any EMD technique are the following:

1) Extrema detection.
2) Envelope estimation.
3) Evaluation of a stoppage criterion.

These steps are straightforward in the standard EMD algorithm that deals with only one variable. However, when considering multidimensional or multivariate data, the complexity of performing these steps increases substantially. It has already been demonstrated that the fast and adaptive algorithm is well suited to multidimensional data [24,37]. Naturally then, this is the initial approach one would take in order to perform multivariate analysis of multidimensional signals. Such a fast and adaptive multivariate, multidimensional EMD processing method is outlined in Algorithm 1 and an explanation follows. First, note that the dimensionality of each element (each channel) of the vector v is not explicitly mentioned, since the method is applicable to multidimensional signals. Second, the computational effort of Steps 2 and 3 in Algorithm 1 for multidimensional signals is greatly reduced by utilizing Delaunay triangulation and separable filters [37]. Finally, the summation in Step 6 must take place over the entire domain of the multidimensional signal (only one summation symbol was placed to maintain generality). A tolerance value of 0.1% of the signal amplitude (smallest between channels) prescribed in Step 6 usually leads to good results and avoids oversifting.

Algorithm 1: Fast and Adaptive Multivariate EMD (FA-MVEMD)

1. Set each channel of the multivariate signal $\{\boldsymbol{v}_i\}_{i=1}^{n}$ to h_i.
2. Project the multivariate signal $\{\boldsymbol{h}_i\}_{i=1}^{n}$ onto a unit vector whose direction cosines are all equal to $1/\sqrt{n}$.
3. Find *both* the maxima and minima of the projected signal, p^{θ_k}.
4. Determine the window size for the order statistics filter by considering the distances between extrema.
5. Calculate the maximum and minimum envelopes, $e_{max,i}$ and $e_{min,i}$, and consequently the mean envelope, m_i, for each channel 'i' using a maximum and minimum order statistics filter, respectively, of the *same window size* across all channels.
6. Extract the 'detail' for each channel, d_i, using $d_i = h_i - m_i$. If *every* 'detail' d_i fulfills the stoppage criterion

$$\frac{\sum m_i^2}{\sum h_i^2} < \mu \text{ (tolerance)}$$

set $h_i = v_i - d_i$ and proceed, otherwise set $h_i = d_i$ and go to Step: 5

7. Perform Steps: 2-6 for a predetermined number of modes or until all oscillatory content is removed.

For the purpose of easy visualization, consider Fig. 8 to discuss a simple example application of a 1D multivariate signal. By performing a projection of these two channels with variable projection angle (Fig. 9), it is evident that in any direction of projection that contains contributions from both channels, either the maximum envelope or the minimum envelope of the highest frequency channel (Channel 2) is captured. The average of a large number of directions uniformly distributed on the circle eventually gives the mean envelope. The same mean envelope can be produced by considering only one direction of projection that contains contributions from both channels (say equal contributions). However, both the maximum and minimum envelopes of this projection must be identified to produce the mean envelope. So, in the bivariate case a suitable direction would be $\theta = \pi/4$, where the direction cosines are given by $\cos \pi/4 = 1/\sqrt{2}$ and $\sin \pi/4 = 1/\sqrt{2}$. Using the extrema obtained from this projection, a window size can be determined using the methods outlined in [24] or [37]. This window size is then used to obtain the mean envelope and consequently extract a bivariate IMF, including contributions from each channel. Since the window size, which serves as the parameter that controls the scale of the extracted IMF, is fixed across all channels, mode alignment is automatically achieved.

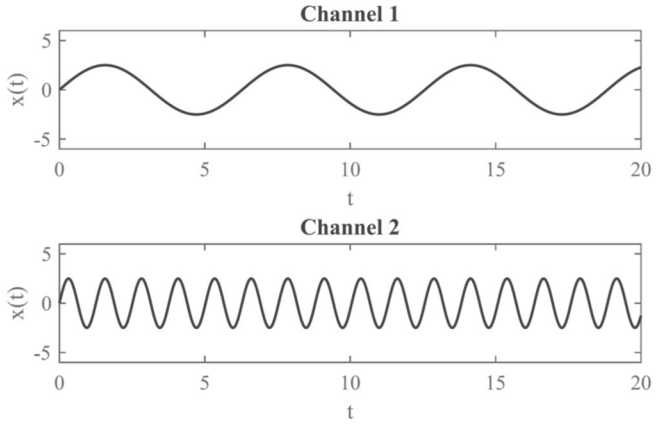

Fig. 8 Example 1D bivariate signal.

As an example of the application of this algorithm, synthetic signals with multiple frequency modes (2, 8, and 16 Hz) were decomposed with conventional multivariate EMD [33] as well as fast and adaptive multivariate EMD. The results are shown in Fig. 10 and Fig. 11. The computation times for MEMD [33] and the FA-MVEMD algorithm of the current study on an Intel(R) Xeon(R)W-2133 CPU@3.6 GHz are given in Table 1. It can be seen that the fast and adaptive method shows and order of magnitude decrease in computation time. The

reconstruction error produced after summing the residue and IMFs was at machine precision for both methods. This is expected since EMD forms a complete basis.

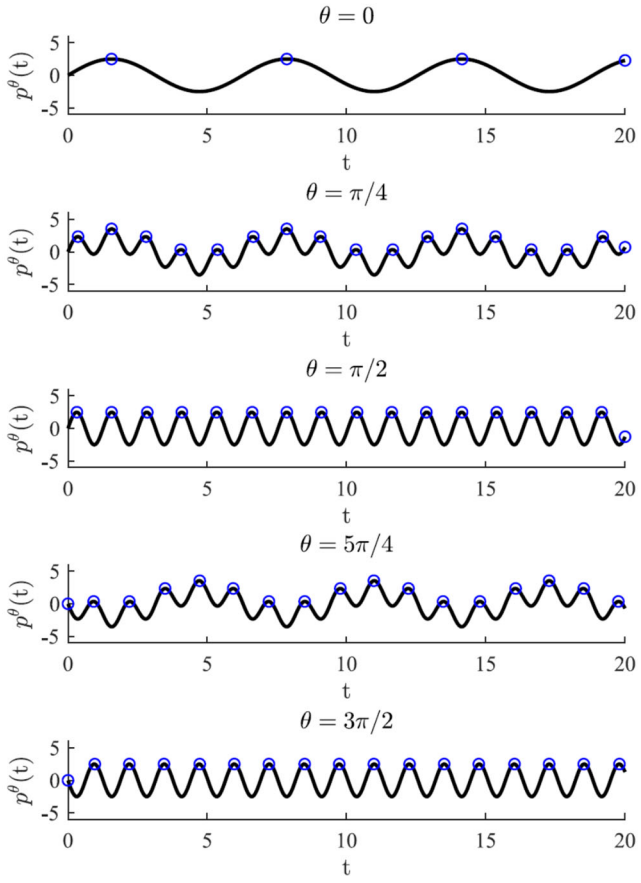

Fig. 9 Projection of bivariate signal across multiple projection directions (θ).

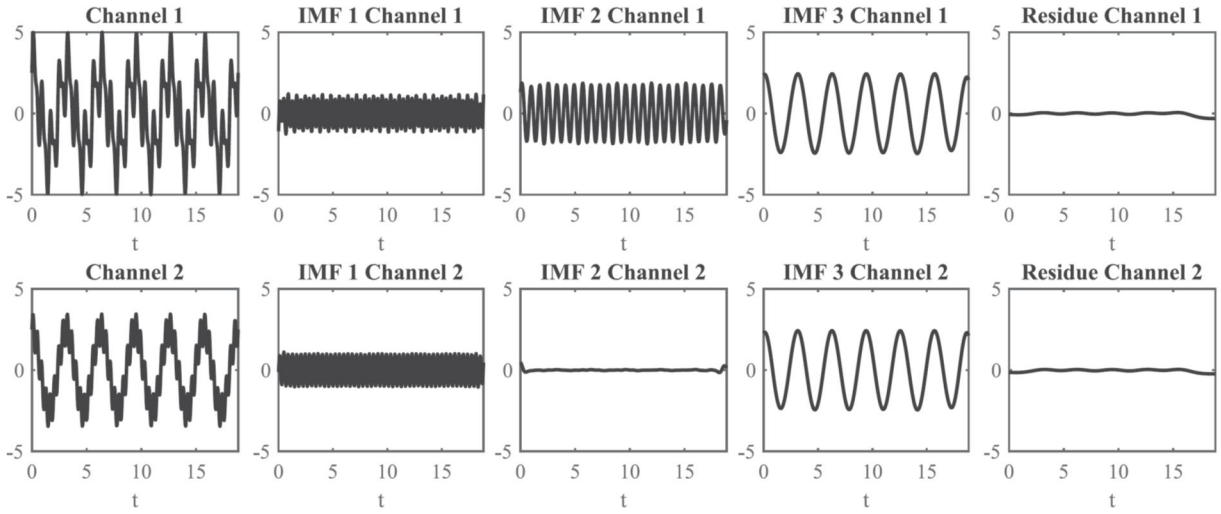

Fig. 10 Conventional multivariate EMD (MEMD).

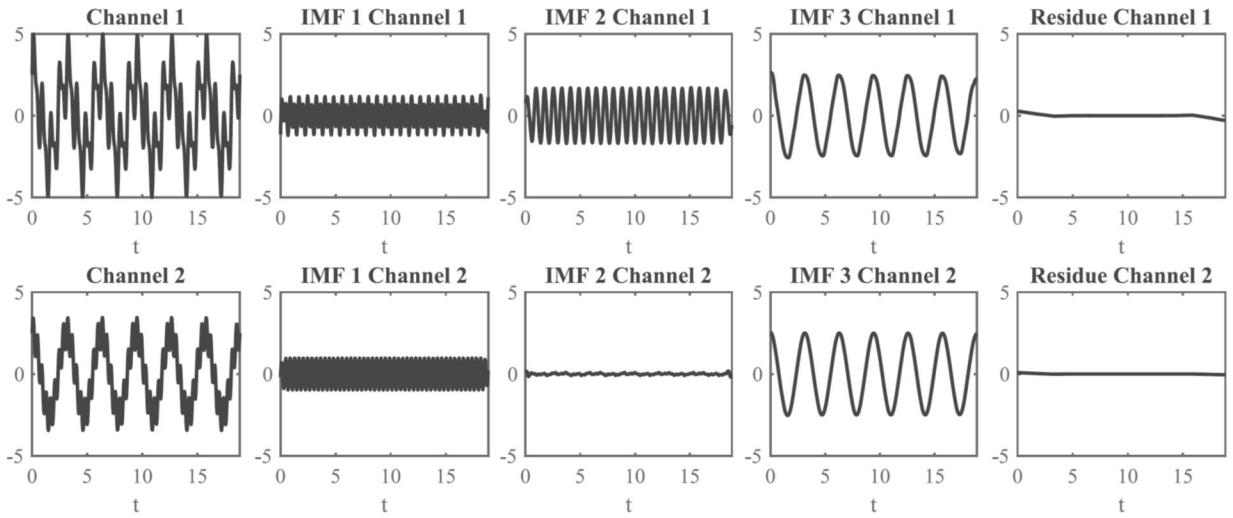

Fig. 11 Fast and adaptive multivariate EMD (FA-MVEMD).

Table 1 Comparison of computation times between MEMD and FA-MVEMD.

Channels (Directions)	3 (6)	6 (12)	12 (24)	16 (32)
MEMD	0.3670 s	0.9012 s	1.6860 s	2.7492 s
FA-MVEMD	0.0426 s	0.0856 s	0.1590 s	0.2048 s

An additional example is shown for a multivariate signal in 3D. Similar to the 1-D case, synthetic texture images were decomposed using FA-MVEMD. The textures were generated with the following components: $f_1 = \sin 3.5x + \sin 3.5y + \sin 3.5z$; $f_2 = \sin x + \sin y + \sin z$; $f_3 = \cos x/24 + \cos y/24 + \cos z/24$.

1) Channel 1: $f_1 + f_2 + f_3$.
2) Channel 2: $0 + f_2 + 0$.
3) Channel 3: $0 + 0 + f_3$.

The results are shown in Fig. 12. f_1 is extracted in Channel 1 only, f_2 is extracted in Channels 1 and 2 only, and f_3 is present in Channels 1 and 3. The computation time for a decomposition of 3 channels of size 100 × 100 × 100 each, was about 180 s. The authors also achieved similar results for trivariate 2D synthetic texture images, but the results have been excluded here for the sake of brevity. With the use of a simple synthetic signal, these results demonstrate the functionality of the FA-MVEMD algorithm developed in the current study.

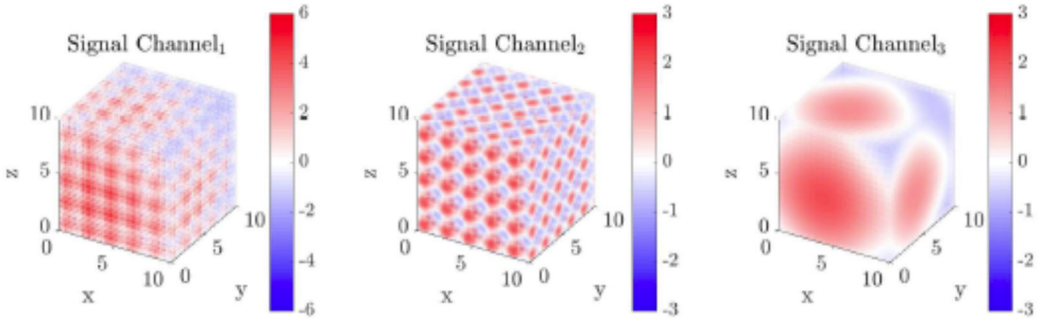

(a) Original signal.

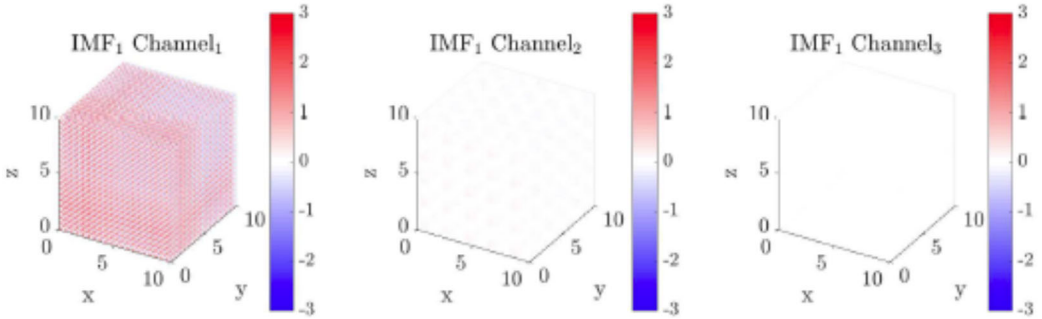

(b) IMF_1

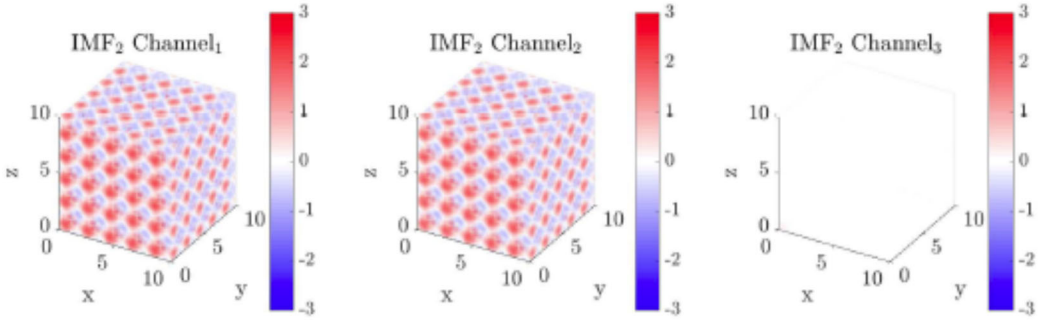

(c) IMF_2

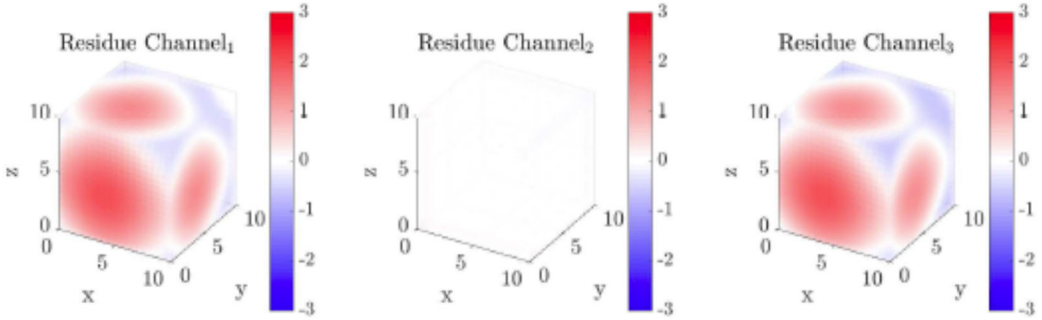

(d) R

Fig. 12 FA-MVEMD for a 3D trivariate signal.

Riesz Transformation and Monogenic Signal

One of the primary goals of the present investigation was to extract the amplitude, A, and the wavelengths, λ_x, and λ_y, associated with a spatially-varying velocity field. The estimation of these parameters was made complicated by the non-trivial spatial variation of the aforementioned quantities, and the intrinsic three-dimensional nature of the velocity field of interest. The instantaneous amplitude and wavelength/frequency for a one-dimensional signal is most commonly calculated using the Hilbert transform.[38,39] In this approach, the Hilbert transform is applied to the acquired signal, $f(t)$, to obtain the transformed signal $f_h(t)$. The Fourier-domain definition of $f(t)$ and $f_h(t)$ are provided in Eq. 3 a) and 3 b). The signals $f(t)$ and $f_h(t)$ form a harmonic conjugate pair and are used as real and imaginary parts to define a complex, analytic signal, $f_a(t)$, as presented in Eq. 4. The instantaneous amplitude, $A(t)$ and the frequency, $f_{inst}(t)$, of the signal $f(t)$ are then calculated directly using Eq. 5 and 6.

$$F\{f(t)\} = H(\omega) \tag{3a}$$

$$F\{f_h(t)\} = -i\frac{\omega}{|\omega|}H(\omega) \tag{3b}$$

$$f_a(t) = f(t) + if_h(t) \tag{4}$$

$$A(t) = |f_a(t)| = \sqrt{f(t)^2 + f_h(t)^2} \tag{5}$$

$$f_{inst}(t) = \frac{1}{2\pi}\frac{d}{dt}\tan^{-1}\left(\frac{f_h(t)}{f(t)}\right) \tag{6}$$

The isotropic generalization of the Hilbert transform was used in order to calculate the desired properties of signals in higher dimensions, based on the work of Felsberg and Sommer.[40] This approach involves the application of Riesz transform to calculate the higher-dimension equivalent to the analytic signal, which is termed as the monogenic signal. The monogenic signal belongs to a class of generalized complex functions, having multiple imaginary components. The number of imaginary components is equal to the number of dimensions associated with the input signal. For an example two-dimensional signal, $f(x,y)$ shown in Fig. 13, the monogenic signal, $f_m(x,y)$, is associated with two imaginary components, as described by Eq. 7. The Fourier domain representations of the imaginary components of the monogenic signal are presented in Eq. 8 a) and 8 b). Similar to the process described in reference to the one-dimension analytic signal, the spatially-varying amplitude for the two-dimensional signal is calculated using Eq. 9. Finally, the angular rotation in three dimensions of the vector defined by the three components of the monogenic signal, $f, f_{m,x}$, and $f_{m,y}$, due to infinitesimal variations in x and y, provides a measure of the wavelengths, λ_x, and λ_y, respectively. This definition is stated more precisely in Eq. 10 a) and 10 b).

$$f_m(x,y) = f(x,y) + if_{m,x}(x,y) + jf_{m,y}(x,y) \tag{7}$$

$$F\{f_{m,x}(x,y)\} = \begin{cases} -i\dfrac{\omega_x}{|\bar{\omega}|}H(\bar{\omega}), & \bar{\omega} \neq 0 \\ 0, & \bar{\omega} = 0 \end{cases} \tag{8a}$$

$$F\{f_{m,y}(x,y)\} = \begin{cases} -i\dfrac{\omega_y}{|\bar{\omega}|}H(\bar{\omega}), & \bar{\omega} \neq 0 \\ 0, & \bar{\omega} = 0 \end{cases} \tag{8b}$$

$$A(x,y) = |f_m(x,y)| = \sqrt{f(x,y)^2 + f_{m,x}(x,y)^2 + f_{m,y}(x,y)^2} \tag{9}$$

$$\frac{1}{\lambda_x} = \frac{1}{2\pi}\lim_{\Delta x \to 0}\frac{1}{\Delta x}\cos^{-1}\left(\frac{\overline{f_m(x+\Delta x,y)}.\overline{f_m(x,y)}}{\left|\overline{f_m(x+\Delta x,y)}\right|\left|\overline{f_m(x,y)}\right|}\right) \tag{10a}$$

$$\frac{1}{\lambda_y} = \frac{1}{2\pi}\lim_{\Delta y \to 0}\frac{1}{\Delta y}\cos^{-1}\left(\frac{\overline{f_m(x,y+\Delta y)}.\overline{f_m(x,y)}}{\left|\overline{f_m(x,y+\Delta y)}\right|\left|\overline{f_m(x,y)}\right|}\right) \tag{10b}$$

As an example, the spatially-varying amplitude, $A(x,y)$ and the wavelengths, λ_x, and λ_y, for the signal $f(x,y)$, was calculated using Eq. 7–10. The amplitude field is presented in Fig. 14 a). For additional clarity, a slice of $f(x,y)$ along the right diagonal is presented as a solid black curve in Fig. 14 b). The orientation of the diagonal is indicated by a dashed line, '*r*' in Fig. 13 and Fig. 14 a). The corresponding slice of the amplitude field is also presented in Fig. 14 b) using a solid blue curve.

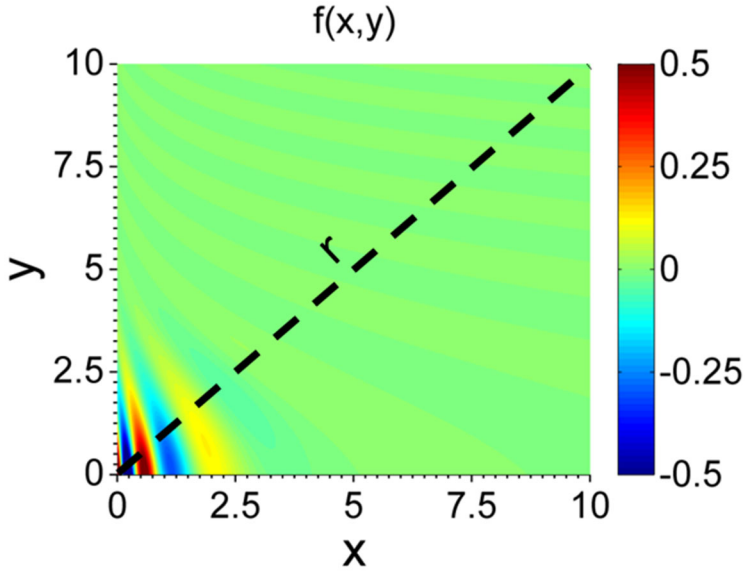

Fig. 13 Example two-dimensional signal, *f*(*x*,*y*). Dashed black line, 'r', represents the directional slice of *f*(*x*,*y*).

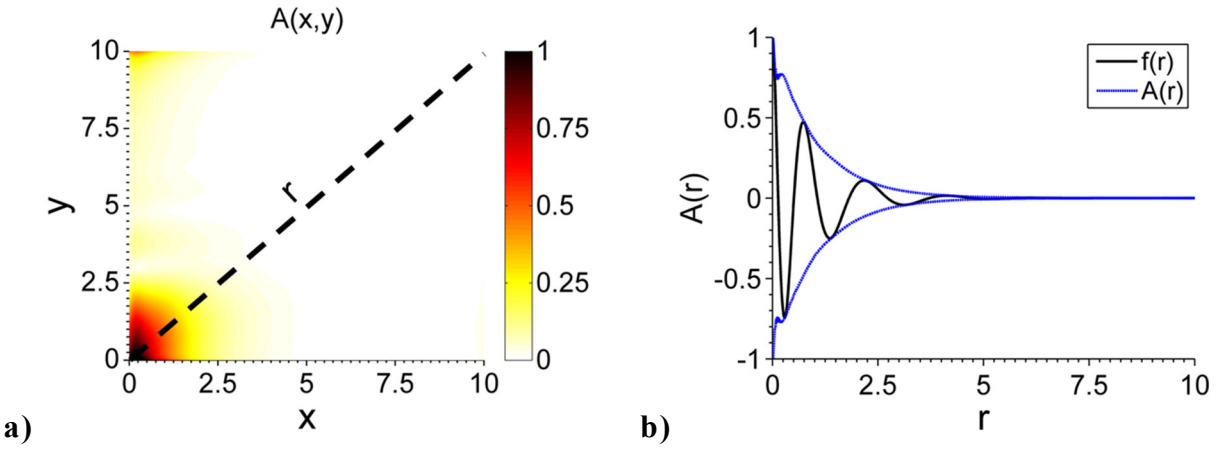

Fig. 14 a) Amplitude field, *A*(*x*,*y*), associated with the example function, *f*(*x*,*y*), from Fig. 13, and b) Slices of *f*(*x*,*y*) and *A*(*x*,*y*) along the direction '*r*'.

From Fig. 14 b), the amplitude is found to provide an accurate representation of the functional envelope of $f(x,y)$ along the diagonal, 'r'. The λ_x and λ_y fields corresponding to $f(x,y)$ are presented in Fig. 15 a) and b), respectively. Slices of the wavelengths were also extracted at fixed x and y locations as indicated by the dashed lines in Fig. 15 a) and b). While the λ_x slice was extracted at $y_0 = 5$, the λ_y slice was extracted at a fixed $x_0 = 5$. The variation in these slices is presented using black curves in Fig. 16 a) and b), respectively. The corresponding 'real' wavelength variations, which were used in the analytical definition of the function, $f(x,y)$, are presented in blue, in Fig. 16 a) and b). The calculated wavelengths, from Eq. 8 a) and b), are found to compare favorably with the predefined 'real' wavelengths.

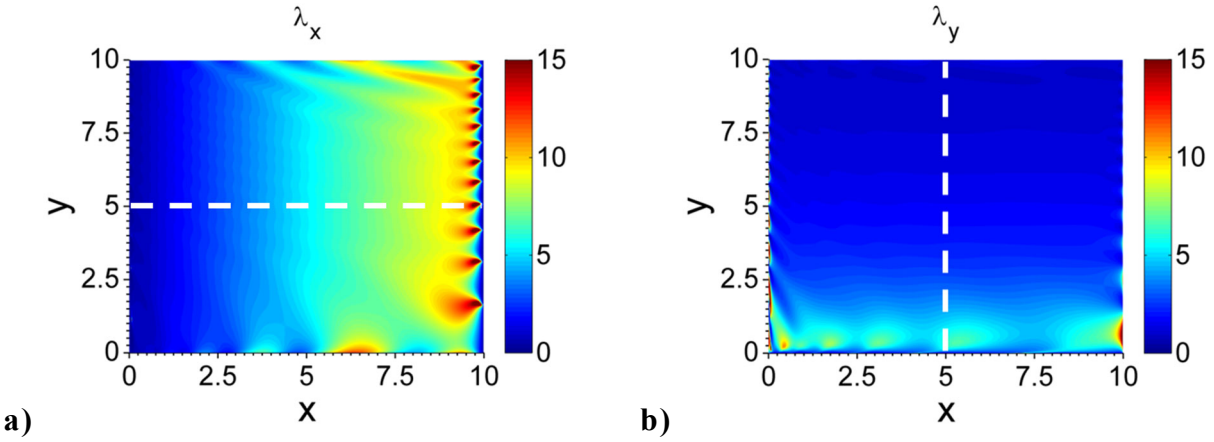

Fig. 15 a) The a) *x* and b) *y* wavelengths corresponding to the function, *f*(*x*,*y*), from Fig. 13. Dashed white lines indicate directions along which slices of the wavelengths were extracted for additional comparison.

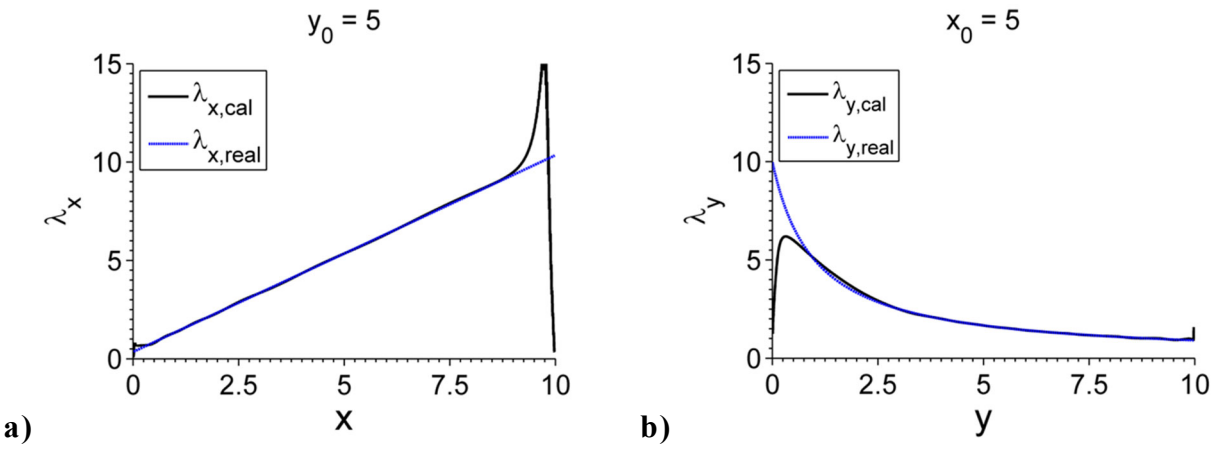

Fig. 16 Slices of a) λ_x at y_0 = 5, and b) λ_y at x_0 = 5 extracted from Fig. 15 a) and b), respectively. The analytical/'real' definitions for the corresponding wavelengths are shown in blue, for comparison.

The results from Fig. 14–16 provided sufficient validation for the use of the monogenic signal-based technique for the estimation of the amplitude and wavelength fields associated with spatially-varying velocity fields of interest.

Modal Analysis of Transitional Flow

Experimental Velocity Field and POD Analysis

An example sequential set of streamwise velocity fluctuations obtained from these TR-PIV data are shown in Fig. 17, demonstrating the ability to capture a controllable, time-dependent set of velocity measurements of the breakdown portion of the natural transition process. Additional basic statistical features of the boundary layer flow are illustrated in Fig. 18. The mean streamwise velocity field shows a typical developing boundary layer; however, higher-order statistics, such as turbulence kinetic energy [$TKE = \frac{1}{2}\left(\overline{u'^2} + \overline{v'^2}\right)$] and Reynolds shear stress ($RSS = -\overline{u'v'}$), exhibit a region of increased levels across the region from x = 0.03 to x = 0.085 [see Fig. 18 (b) and (c)]. Selected vertical profiles of these quantities using inner units, i.e., $y^+ = y/u_\tau$ and $u^+ = u'/u_\tau$, where $u_\tau = \sqrt{\tau_w/\rho}$ is the local friction velocity, and τ_w and ρ are the local wall shear stress and fluid density, are shown in Fig. 19 (a), Fig. 19 (c), and Fig. 19 (d) to further illustrate their evolution across the laminar-turbulent transitional region. Due to the inherent trade-off between FOV size and spatial resolution used in the current experiment, it was not feasible to include the unperturbed laminar boundary layer in the spatial domain of the time-resolved vector fields. As a result, a slight departure from the canonical laminar flow velocity profile is already observed at x = 0.02 m ($Re_x = 2.02 \times 10^5$). The peak of the RSS and TKE ($y^+ \approx$ 25–30) increased with streamwise distance, reaching maximum values at x = 0.08 m ($Re_x = 2.1 \times 10^5$). Further downstream, a decrease in the peak RSS and TKE is observed, which converged to classical turbulent correlation profiles across the downstream end of the PIV field of view.

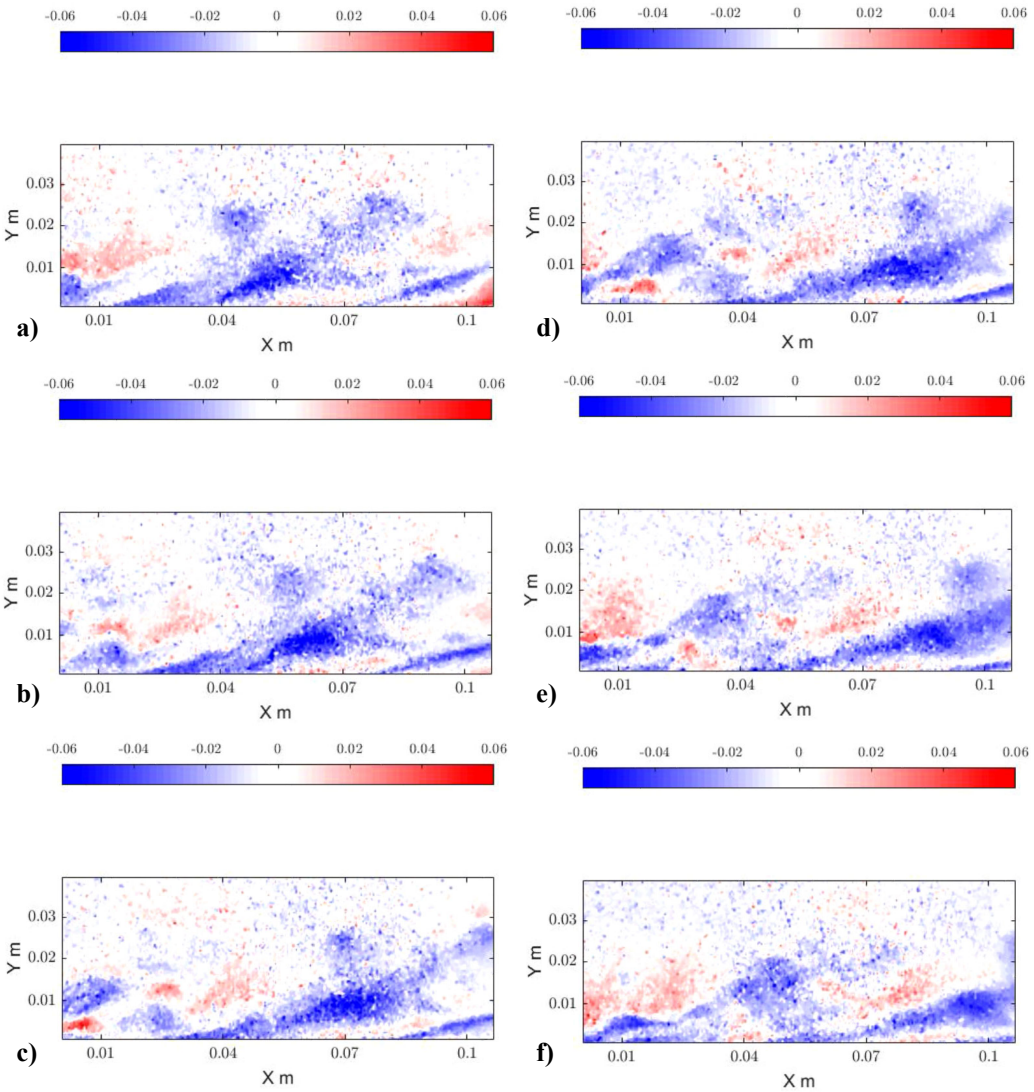

Fig. 17 Streamwise velocity fluctuations obtained from planar, two-component TR-PIV data acquisition, a) $t = 0$, b) $t = 0.16$ sec, c) $t = 0.32$ sec, d) $t = 0.48$ sec, e) $t = 0.64$ sec, f) $t = 0.80$ sec.

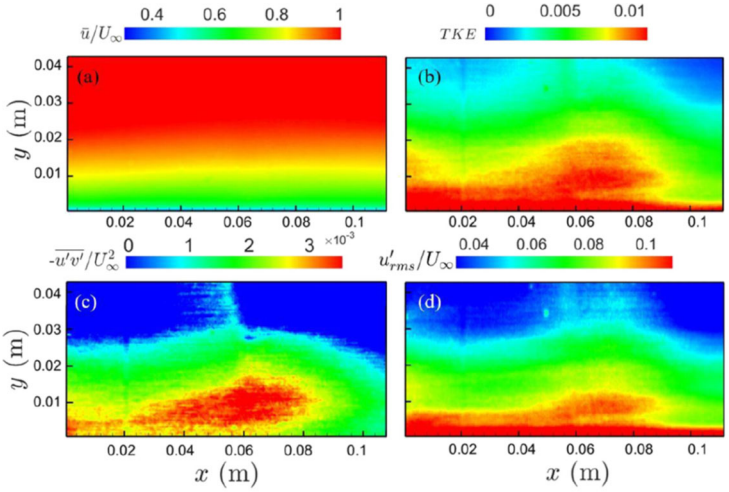

Fig. 18 (a) mean velocity U/U_∞, (b) TKE, (c) RSS, and (d) streamwise turbulence intensity I_u.

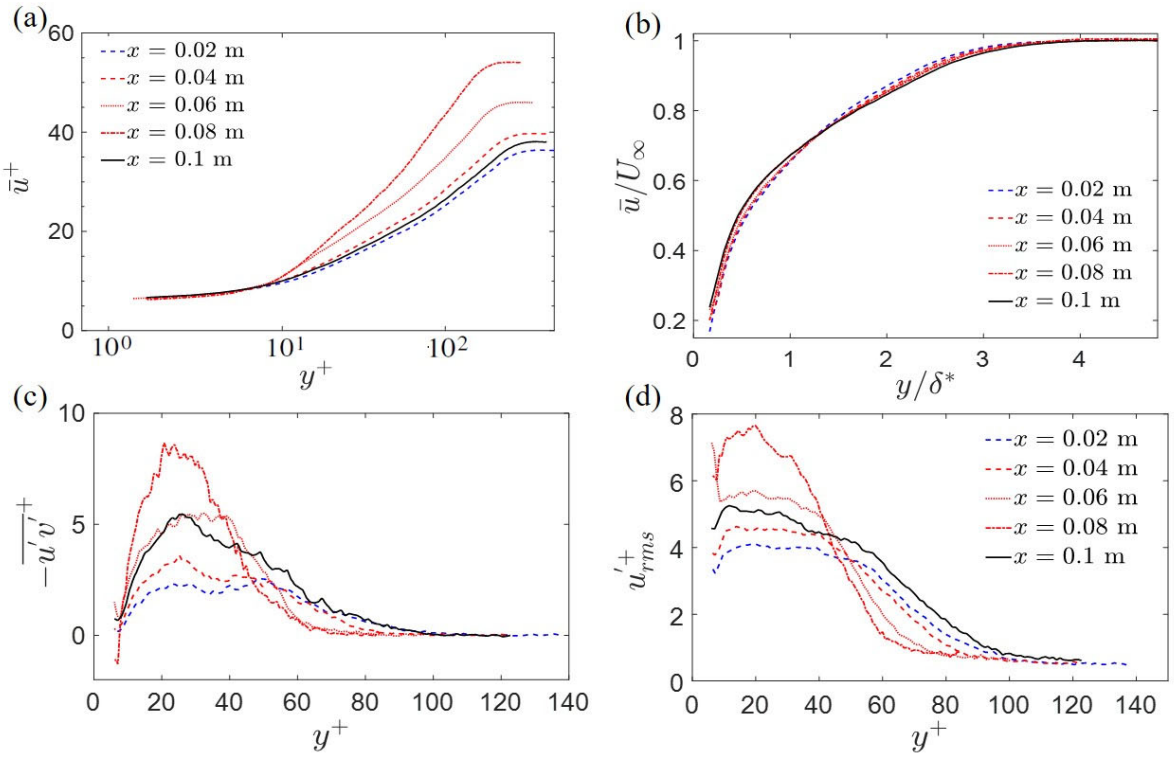

Fig. 19 Transitional boundary layer velocity profile and turbulence statistics.

The presence of a local overshoot region in the mean velocity and turbulent statistics near the wall observed in Fig. 19 is consistent with the skin-friction overshoot produced during the late stages of boundary transition observed in previous DNS and experimental literature.[41-44] According to Sayadi et al.,[1] the initial departure from the laminar regime occurs with the formation of Λ vortices inherent to the natural boundary-layer transition process. Fig. 18 and Fig. 19 suggest the presence of coherent structures that provide a dominant contribution to the turbulent fluctuations throughout the transition process, as observed through locally increased values of RSS and TKE.[45,46] After the initial formation near the wall, these vortices moved away from the wall with increased streamwise distance, creating the characteristic Λ vortex shape around $x = 0.015$ m ($Re_x = 2 \times 10^5$).

The energy contribution of the first 40 modes obtained through POD analysis of the time-resolved velocity vector fields is shown in Fig. 20. The first mode contributes about 6% of the total turbulence kinetic energy, with relatively slow convergence observed in the mode energy spectrum. The first ≈35 modes contribute ≈50% of the total TKE, demonstrating a rather complex flow produced by the transition process. The spatial mode shapes associated with the first six streamwise POD modes $\varphi_{u'}$ are shown in Fig. 21. These mode shapes demonstrate structural features consistent with those of horseshoe or hairpin vortices, which have been widely recognized in wall-bounded flows after first proposed by Theodorsen.[47,48] The POD modes shown in Fig. 21 were inspected to determine their relation to characteristics of known coherent structures, beginning with the inclination angle, β, of spatial features observed in the POD modes; this is defined as the angle between the structure center line and the horizontal plane.[49]

The velocity fluctuations attributed to mode 1 exhibited an inclination angle, $\beta_1 \approx 7$ deg, across nearly the entire spatial domain interrogated [Fig. 21 (a)]. Similarly, the velocity fluctuations attributed to modes 2 and 3 exhibited a similar inclination angle β_1 away from the wall, which upon reaching $y = 0.01$ m transitions into an upper section with an inclination angle, $\beta_2 \approx 25$ deg, between $y = 0.01$ m and $y = 0.02$ m [Fig. 21 (b) and (c)]. Distinct angles, $\gamma = 15$ deg and $\gamma = 14$ deg, for the vortex packet[50] are noted in modes 5 and 6 [Fig. 21(e) and (f)].

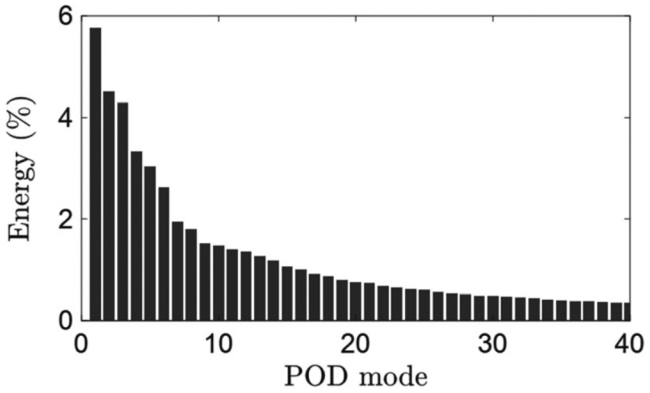

Fig. 20 Energy distribution of POD modes, normalized to total TKE.

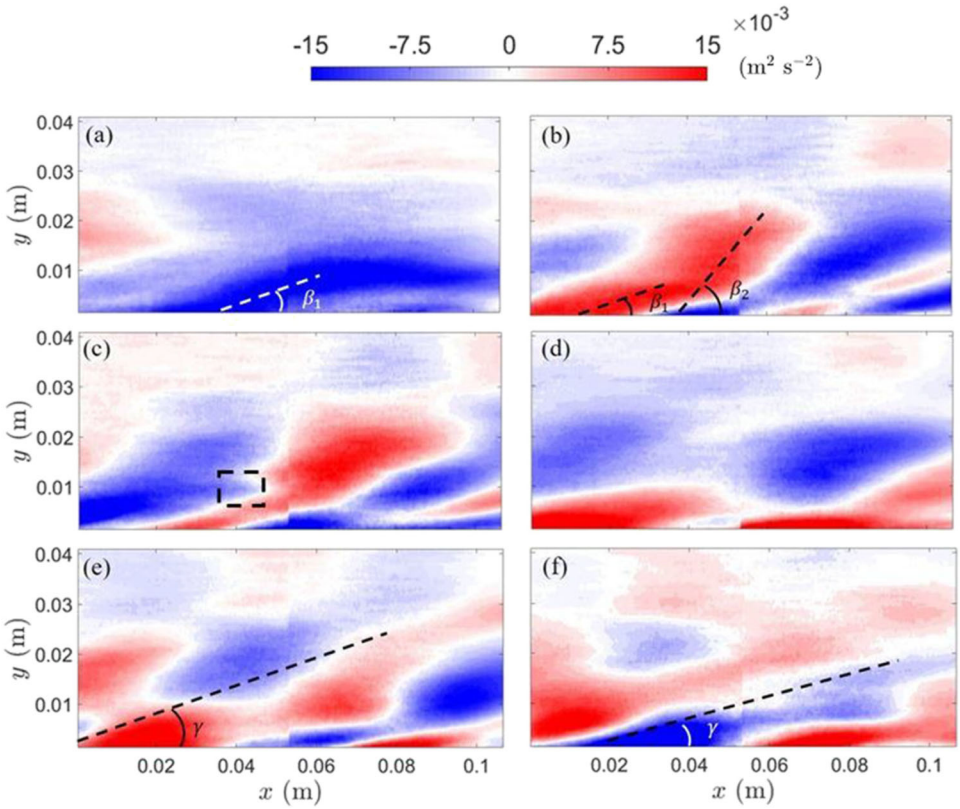

Fig. 21 Spatial organization of the (a) first, (b) second, (c) third, (d) forth, (e) fifth, and (f) sixth POD modes.

In addition to the aforementioned spatial features, the time-dependent amplitudes, $a_n(t)$, of the POD modes provide distinct characteristics consistent with known coherent structures; see Fig.

22 (a) and Fig. 22 (b). The first three modes are associated with a single sinusoidal-like cycle at a consistent frequency, suggesting a correlation to a common flow feature between these primary modes. This commonality is contrasted with the higher modes, where multi-scale flow structures are expected due to nonlinear interactions, such as sub-harmonic and super-harmonic excitation.

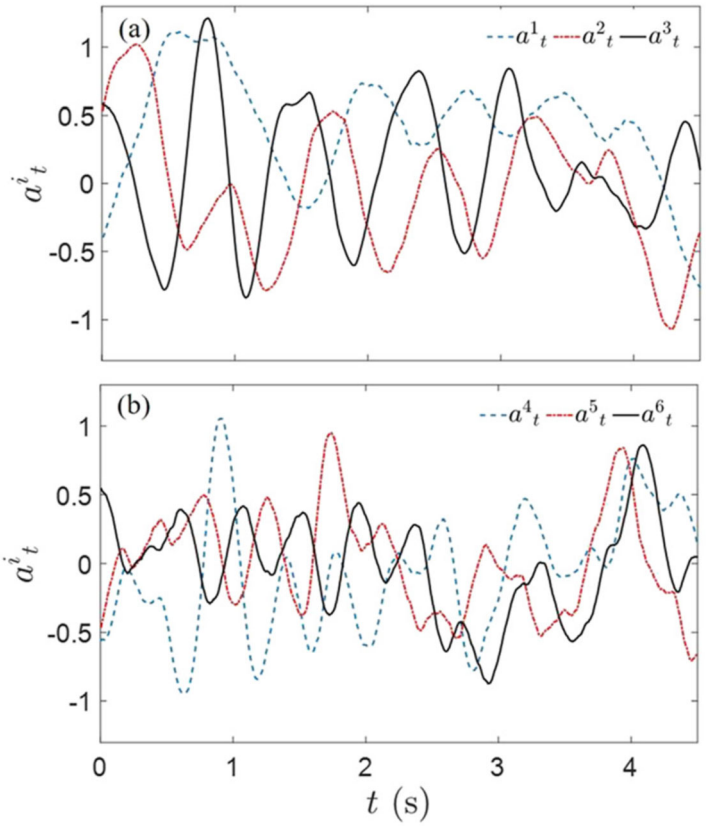

Fig. 22 Time-dependent POD coefficients for: (a) modes 1-3, (b) modes 4-6.

The observations indicate that the first three modes are associated with the development of a single primary hairpin vortex (PHV).[46] A distinct pattern in mode 4 appears to follow a similar scale as the PHV development observed across the first three modes. Still, this mode indicates a reversal in the perturbation velocity direction of the mode shapes across the hairpin head region, which might be attributed to the difference of convection speed between the near wall and the outer region. However, a clear distinction of the flow scales observed in modes 5 and 6 to the first four modes can be seen in Fig. 21. Instead of a single hairpin vortex, the higher modes (≥5) are conjectured to be associated with a hairpin packet, with the nesting angle γ in agreement with literature (12 deg ≤ γ ≤ 20 deg for hairpin vortex packets[50-53]). The hairpin vortex packet is known to form once the initial PHV amplitude exceeds a certain threshold.[45] These hairpin packets consist of self-similar secondary and tertiary hairpin vortices that form downstream of the PHV as a result of nonlinear interactions produced across the later stage of transition.[45,52]

To further correlate the underlying spatial characteristics of the modes produced by the current POD analysis with flow interactions produced by coherent structures, those produced by modes 1 and 2 are shown in Fig. 23 (a) and Fig. 23 (b) with a superimposed distribution of velocity

vectors. It should be noted that the time-dependent mode amplitudes can be positive or negative, so the specific directionality of the mode influence on the dimensional velocity can be either in the direction indicated or in reverse, relative to the vectors shown. The vector field corresponding to the first mode presents a high-amplitude ejection event ($u' < 0$ and $v' > 0$), which is caused by the interaction between the near-wall, low-speed flow that is pumped away from the wall, and the relatively high-speed, freestream flow.[54] Given that the mode amplitude was predominantly positive, this ejection behavior was observed in mode 1 far more frequently than related sweep events. Conversely, the second POD mode takes the form of a coupled sweep and ejection events, showing the reversed streamwise directionality between the upstream and the downstream flows.

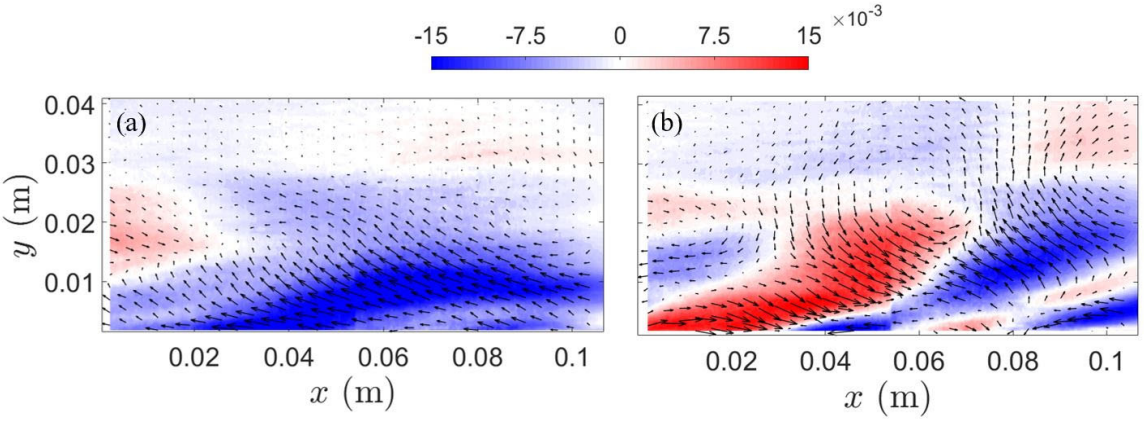

Fig. 23 First two POD modes showing the emergence of low-speed streaks and large-scale sweep/ejection events.

One item specifically studied using the 2D PIV data is the mechanism associated with skin friction overshoot commonly observed at the conclusion of the laminar-turbulent transition process. This overshoot can be observed in the velocity profile and turbulence statistics presented in Fig. 19. Here, it can be seen that the peak value of Reynolds shear stress grows with streamwise distance, reaching a maximum at x = 0.08 m, and then subsequently decreases by x = 0.10 m, which is sustained throughout the turbulent boundary layer. A similar behavior is commonly observed in the transitional flow literature. In order to better understand the physical mechanisms associated with this phenomenon, a POD reduced-order model was developed. The identification of low-speed streaks and large-scale sweep and ejection events can be observed in the first two modes in Fig. 23. Detection of the peak Reynolds shear stress from the time-resolved PIV data at x = 0.08 m also permitted the use of a conditional averaging technique to identify the flow characteristics reproduced by the reduced-order model preceding and following a local excursion in shear stress. The resulting reduced-order model of the velocity field coinciding with an excursion in Reynolds shear stress is shown in Fig. 24.

The first four POD modes were identified as being the most significant contributors to the overshoot mechanism in the Reynolds shear stress, so these modes were utilized to reconstruct the mean velocity profile and turbulence statistics, similar to those shown in Fig. 19. The

resulting Reynolds shear stress profiles produced by the first three modes are shown in Fig. 25 a), and those produced when using the remaining modes are shown in Fig. 25 b). The peak value of Reynolds shear stress produced in Fig. 25 a) coincides with 83% of the overall amplitude of the actual peak shown in Fig. 19, even though the first four modes only contribute 16% of the turbulent kinetic energy to the flow. Conversely, all of the subsequent higher POD modes do not significantly contribute to the Reynolds shear stresses near the wall, with their effects primarily observable farther from the wall, around $y^+ = 60$.

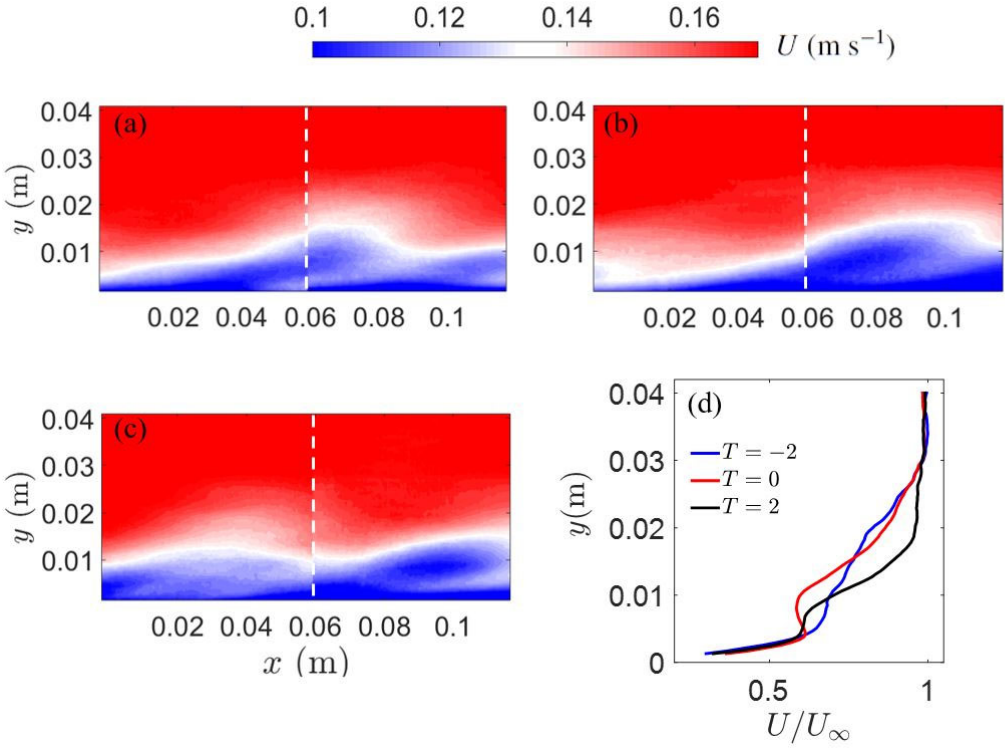

Fig. 24 Reduced-order model before and after the Reynolds stress peak instant (T = 0) using the first four POD conditionally averaged mode coefficients superimposed with the mean velocity. The flow is shown in (a) T = -2, (b) T = 0, (c) T = 2 and (d) their corresponding velocity profile taken at x = 0.08 m.

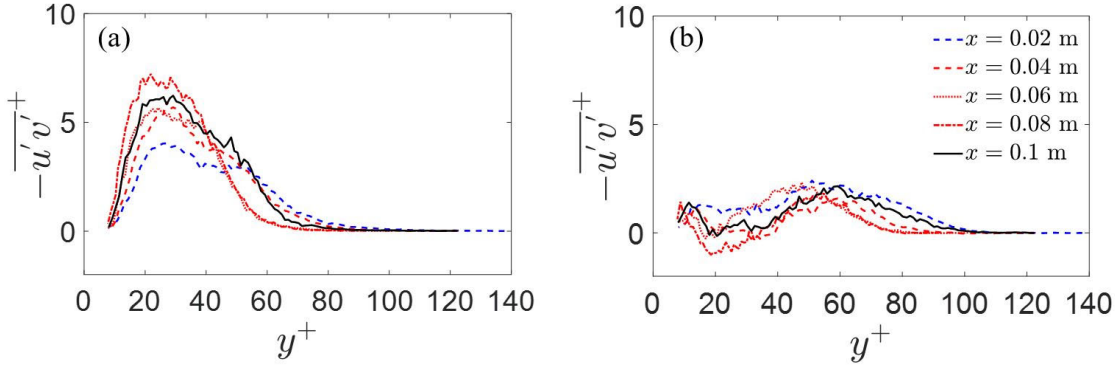

Fig. 25 Reynolds shear stress profiles reconstructed using: a) first four POD modes, b) remaining POD modes.

FA-MVEMD Process and Fourier Decomposition of Transitional Flow

With initial knowledge formed concerning the overall topology and modal representation using conventional decomposition methods, additional detailed study was conducted using the scale-based adaptive EMD methods and Riesz transform/log-Gabor filter analysis methods. The FA-MVEMD approach was utilized on DNS data from Sayadi et al.[1] of K-type boundary-layer transition. A sample snapshot of the Q-criterion field of the original dataset is shown in Fig. 26.[1] For generality, the application of the FA-MVEMD method will simply be implied as the method of choice to perform EMD on the transitional flow dataset in the subsequent discussion. After performing EMD on the three-dimensional, trivariate (u, v, and w) input signal, a total of six IMFs were produced. In order to visualize the vortical flow structures corresponding to these modes, the Q-criterion was calculated for each IMF. The resulting isosurfaces are shown in **Fig. 27**, which are colored by the corresponding average streamwise velocity. Inspection of **Fig. 27** reveals an array of vortical flow scales, from small to large, with increasing IMF. Based on the threshold value of Q used to generate **Fig. 27**, the influence of the secondary instability can first be seen in IMFs 5 and 6 at $x/x_0 = 1.9$. These secondary disturbances then form the legs of the classical Λ-shaped vortices of turbulent spots, with the base of the vortex structure originating in IMF 4 at $x/x_0 = 2.55$. An emergence of smaller vortical flow scales can then be observed on top of this base in IMFs 3, 2, and 1, which rapidly form with successive streamwise distance, across the region of $2.6 \leq x/x_0 \leq 2.8$. This process is then repeated and continued across a longer streamwise extent, until the flow becomes fully turbulent across the entire domain, downstream of $x/x_0 = 3.4$.

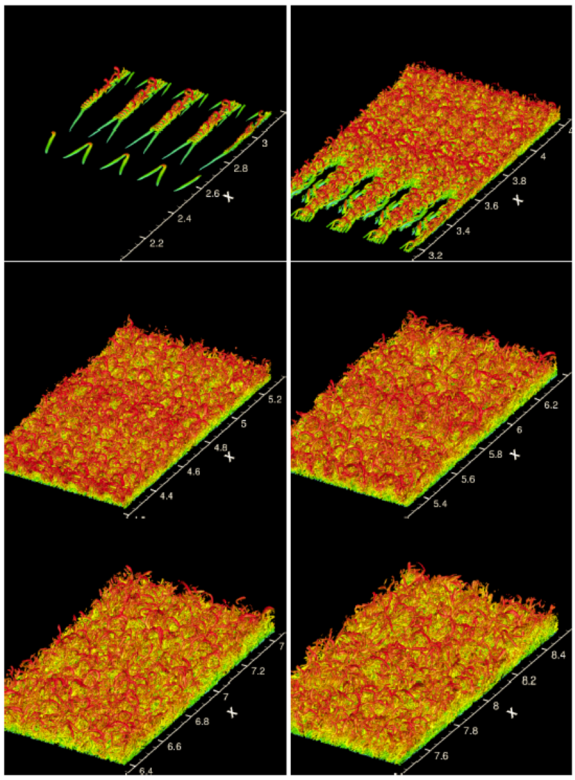

Fig. 26 Q-criterion isosurfaces of K-type transition velocity field (colored by velocity magnitude), after Sayadi et al.[1]

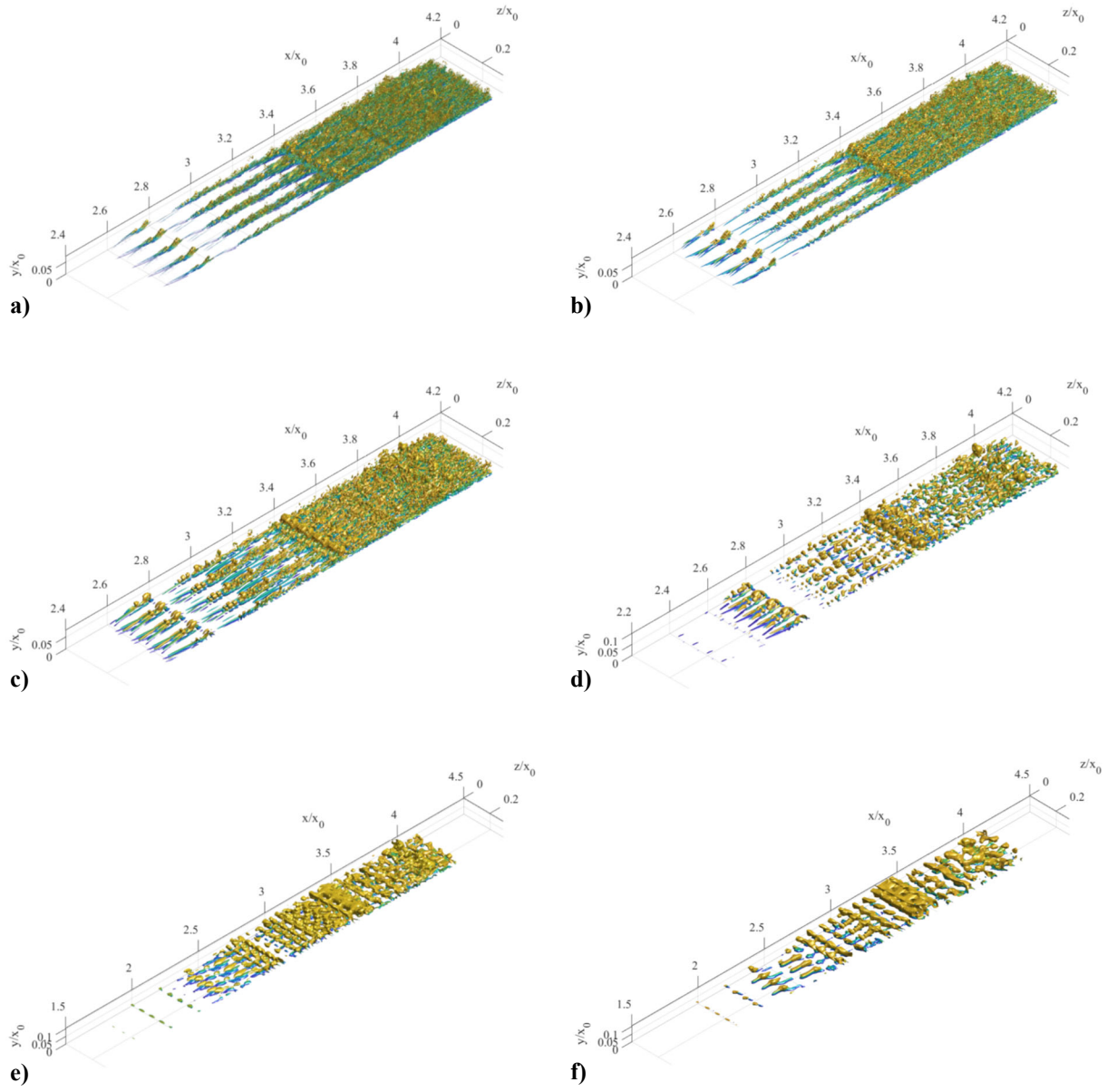

Fig. 27 *Q*-criterion isosurfaces of IMFs, a) IMF 1, b) IMF 2, c) IMF 3, d) IMF 4, e) IMF 5, f) IMF 6.

An analysis of the characteristic spatial scales was also performed to couple to this morphological discussion of the IMF vortex structures identified in **Fig. 27**. Since no direct extensions of Hilbert Spectral Analysis (HSA) for multidimensional EMD existed prior to the filtered Riesz transform developments of the current study, 3D Fast Fourier Transforms (FFT) were first calculated on streamwise windows of each IMF of the u velocity component, as illustrated in Fig. 28. In each window, the result of the 3D FFT was summed radially to obtain a psuedo-power spectral density plot. From **Fig. 29** it can be seen that the TS instability wave has a streamwise non-dimensional wavelength λ/x_0 of about 0.25. This is seen in the power spectrum for IMF 6 shown in **Fig. 29**, corresponding to the early linear region of the transition process. The

length scales produced by the growth of the secondary instability can also be seen in IMF 4, as shown in **Fig. 29** d).

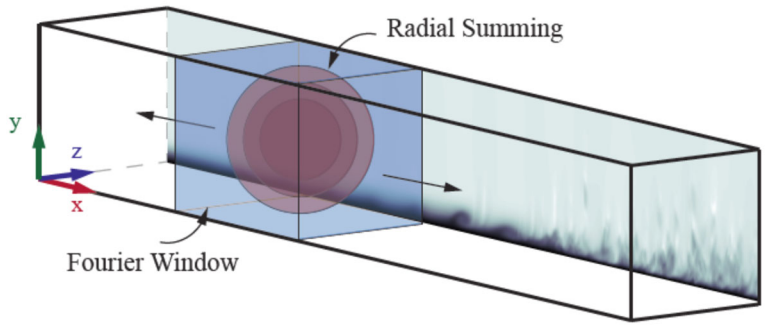

Fig. 28 Illustration of windowed 3D FFT calculation method.

From this growth, the excitation of smaller-scale flow features are produced, as previously seen in **Fig. 27**, though the dominant energy associated with these modes are centered about the secondary instability scale. In this way, the secondary instability acts to modulate the development of these smaller scales, serving as a carrier for the emergence of these smaller turbulent features of the flow. With further streamwise distance, the energy of the smaller scales experience significant growth, resulting in peak amplitudes far greater than the initial TS wave and the secondary instability. However, it is interesting to note that across $3.41 \leq x/x_0 \leq 3.55$ a spectral peak in IMF 6 can still be identified at the original TS wavelength, and with a comparable amplitude to the spectrum produced upstream of this window. Since this region is the initial portion of the flow that would be classically-defined as being "fully turbulent", this observation indicates that the original instability can still be perceptible across a "young" turbulent flow. This observation is also further supported by the spanwise-coherent structures previously observed for IMF 6 in **Fig. 29** across $3.5 \leq x/x_0 \leq 3.8$, though a gradual loss of coherence of these structures can be seen with further increases in streamwise distance. A similar characteristic is also observed in more detailed explorations of the energy content of the transitional flow, as will be discussed later.

Localized Energy Spectra of Boundary-Layer Transition

A principal goal of this study was to calculate and describe the energy spectra associated with fluctuations in the transverse velocity, v and w, in terms of the wavenumber magnitude, $\|k\|$, and the spatial variables x, y, and z. As such, this study provides the first spectral characterization of boundary-layer transition on a flat plate that is localized both in the wavenumber and the physical (spatial) domains. This characterization was achieved through a combination of data-driven modal separation using EMD and three-dimensional signal energy estimation using a filtered-Riesz transformation. The FA-MEMD approach described earlier was utilized to perform multidimensional, multivariate EMD processing, and the filtered-Riesz transform technique was used to understand the spatial distribution of energy across multi-component wavenumber spectra. As step zero in this analysis, the DNS velocity field data of Sayadi et al.[1] for canonical boundary-layer transition process was used.

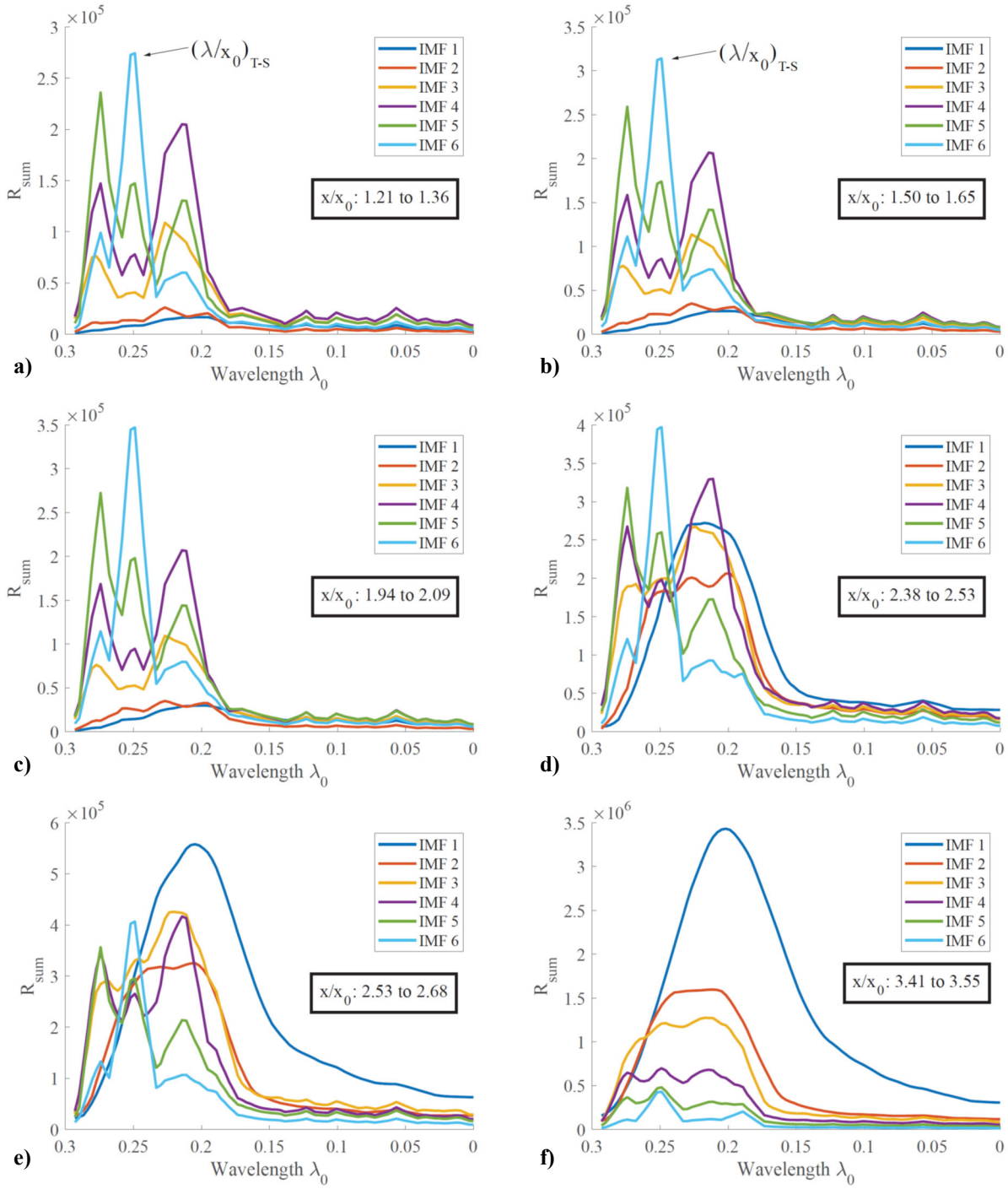

Fig. 29 Windowed 3D FFT spectra of *x*-velocity component across transition process, a) $1.21 \leq x/x_0 \leq 1.36$, b) $1.50 \leq x/x_0 \leq 1.65$, c) $1.94 \leq x/x_0 \leq 2.09$, d) $2.38 \leq x/x_0 \leq 2.53$, e) $2.54 \leq x/x_0 \leq 2.68$, f) $3.41 \leq x/x_0 \leq 3.55$.

A sequence of the streamwise flow morphological development for the K-type transition process is presented in Fig. 30 as isosurfaces of the Q-criterion colored with the streamwise velocity, u. The initial stage of the flow development in Fig. 30 is characterized by a series of Λ vortices which consist of a pair of streamwise-oriented elongated 'legs' with anti-parallel vorticity and a spanwise-oriented vortex 'tip'. It should be highlighted here that the streamwise alignment of the

Λ vortices, as observed in Fig. 30 b), forms a defining feature of the K-type transition process. This flow feature is in contrast with an H-type boundary-layer transition, which is characterized by a staggered distribution of the corresponding vortical structures. The Λ vortices undergo a stretching process, driven primarily by self-induction (Moin et al.,[55]; Bake et al.,[56]; Hambleton et al.,[57]), resulting in the appearance of hairpin-like vortices, as observed between $x/x_0 = 3$ and $x/x_0 = 3.15$. The tips of these hairpin vortices further evolve into ring-shaped Ω vortices, as seen between $x/x_0 = 3.15$ and $x/x_0 = 3.3$. The appearance of the Ω vortices has been associated in the literature (Sayadi et al.,[41]) with high-amplitude fluctuations in velocity and skin friction. Beyond $x/x_0 = 3.3$, the flow is characterized by a web of mutually-interacting hairpin structures with complex, asymmetric geometries as opposed to the symmetric nature of the Λ, hairpin and Ω vortices identified previously. While not shown here for brevity, the collective interactions that appear downstream of $x/x_0 = 3.3$ evolve to produce an organized distribution of hairpin vortices that span across the entirety of the flat plate by $x/x_0 = 3.65$.

As a *first* step in the analysis of the boundary-layer transition spectra, the fluctuations in the velocity components were extracted from the background trend using EMD.

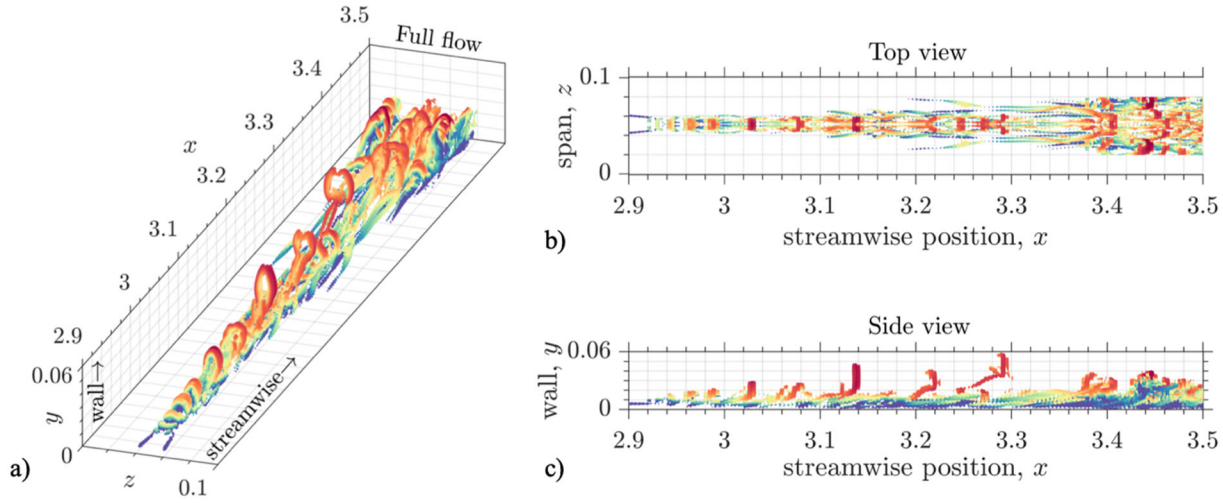

Fig. 30 a) Isometric, b) top, and c) side views of the flow structures during BLT as identified using an isosurface of the Q-criterion colored with the streamwise velocity.

A series of four IMFs, representing pure oscillations about a near-zero mean was extracted simultaneously from each of the three velocity components in 3D using the multi-dimensional, multivariate version of EMD. *Second*, a synthetic signal, $\emptyset$, was defined by taking a projection of the transverse velocity components along a unit vector, $\hat{n}$, perpendicular to the streamwise axis, x, and oriented at an angle of 45 degrees with the wall-normal and the spanwise axes, y and z, respectively:

$$\emptyset = (u + v)/\sqrt{2} \tag{11}$$

As discussed previously in the description of the MV-MEMD method, this choice of unit vector guarantees the inclusion of the smallest-wavelength fluctuations in the synthetic signal described

by Eq. 11. The IMFs corresponding to this signal were derived from the IMFs of the transverse velocities following Eq. 11. Slices in the synthetic signal and the associated IMFs extracted at a fixed spanwise location, $z/x_0 = 0.05$, are presented in Fig. 31. Each contour in Fig. 31 has been normalized with the corresponding in-plane maximum. Due to the nature of the EMD process, successive IMFs in Fig. 31 are associated with increasing wavelength of fluctuations in the synthetic signal. For the *final* step, the amplitudes of these fluctuations were calculated using a filtered-Riesz transform method. In this approach, the raw signal was first processed through a 3D log-Gabor filter in order to localize the signal perturbations in the wavenumber domain. The filtered signal and its corresponding Riesz transform, which provides a generalization of the Hilbert transform in 3D, were then used to extract the spatially-dependent fluctuation amplitude, A, following the principles of monogenic signal analysis described in the literature (Felsberg and Sommer,[40]; Bridge,[58]).

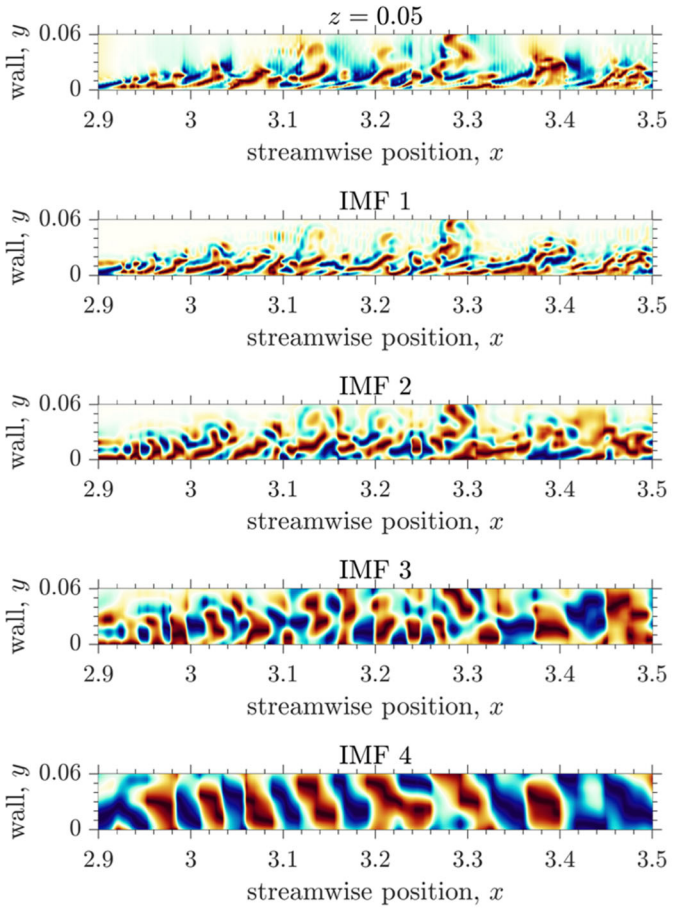

Fig. 31 Slices of the synthetic signal defined by Eq. 1 and the associated IMFs at $z = 0.05$.

The spectra of the transverse velocity fluctuations as embodied in the synthetic signal, $\emptyset$, are presented in Fig. 32. The contours in Fig. 32 describe the distribution of the integrated energy, E_I, as a function of the wavenumber and the streamwise position. This measure of energy was obtained from the signal amplitude using the following equation:

$$E_I = \int_{x_{min}}^{x} \left\{ \int_{y_{min}}^{y_{max}} \left(\int_{z_{min}}^{z_{max}} A^2 \, dz \right) dy \right\} dx \tag{12}$$

where the subscripts 'min' and 'max' refer to the lower and upper bounds of the physical domain. Thus, the integrated energy at a streamwise position, x/x_0, provides a measure of the total energy contained within a region that spans the entirety of the y-z flow domain and extends between the points x_{min} and x along the streamwise direction. It should also be specified that each contour in Fig. 32 has been normalized by the corresponding maximum for the ease of comparison. Select streamwise slices of the integrated energy contours beyond $x/x_0 = 2.95$ are presented in Fig. 33. A full-width three-quarter-maximum (FW3QM) cutoff has been employed in Fig. 33 to highlight the energetic fluctuations in the flow over the artificial broadband noise. The FW3QM energy distributions are observed to span a largely disparate range of wavenumbers with well-defined and distinct peaks, which are identified using black triangles in Fig. 33.

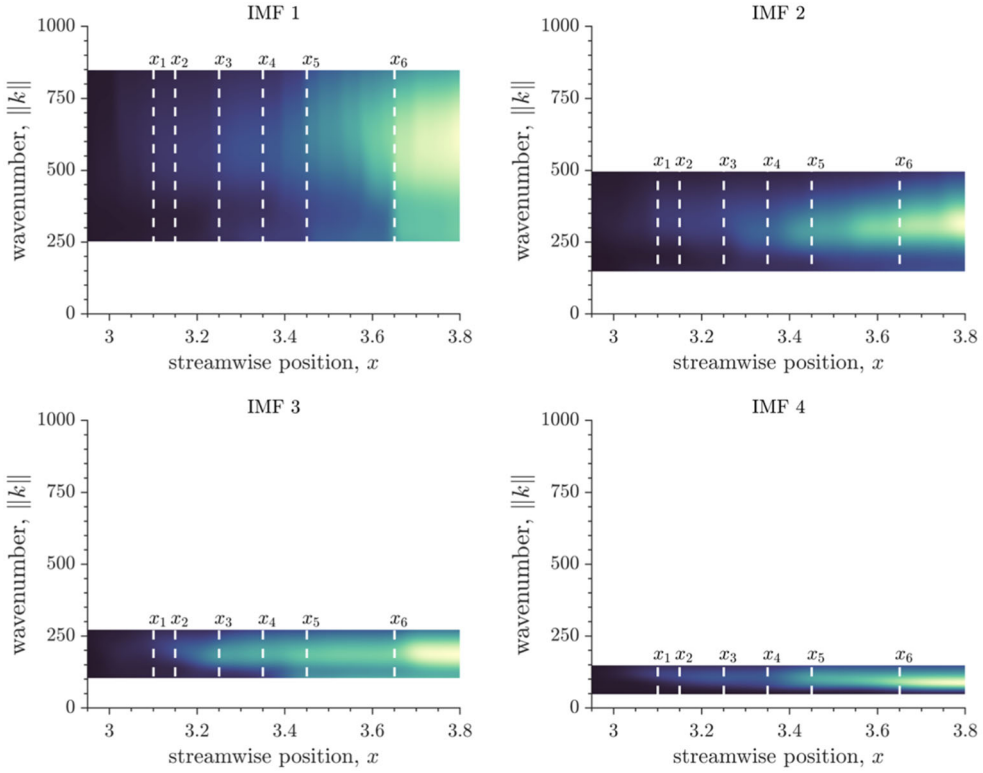

Fig. 32 Wavenumber spectra of the integrated energy associated with fluctuations in the IMFs of the synthetic signal.

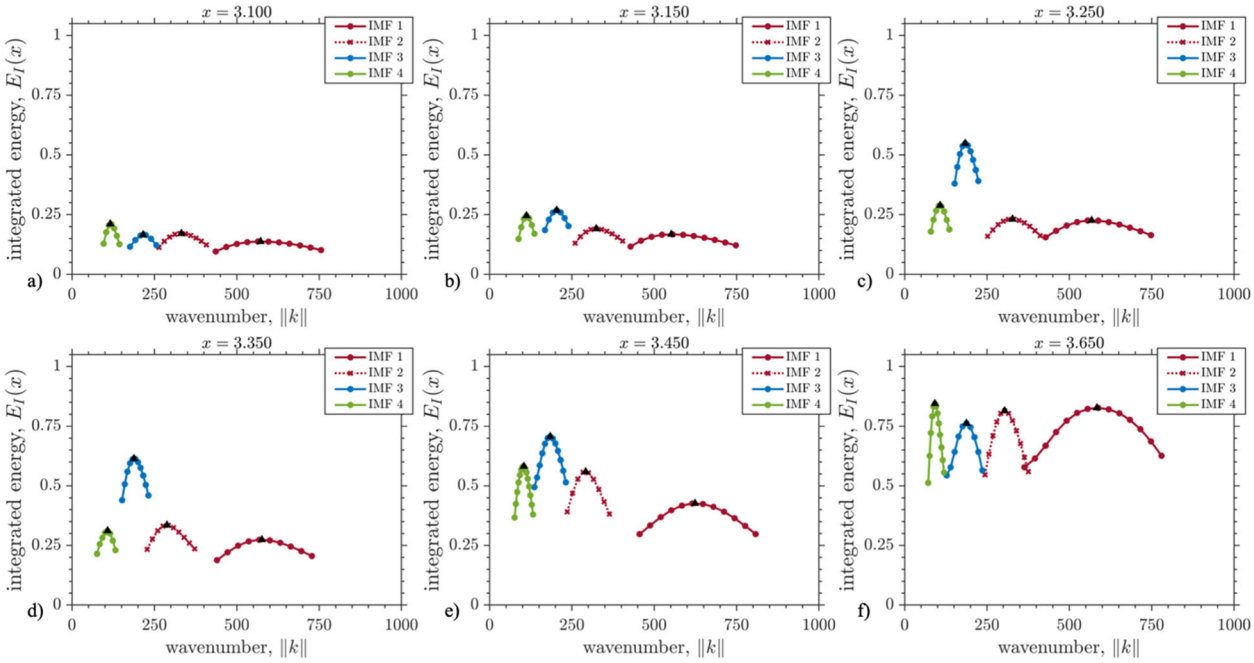

Fig. 33 Full-width three-quarter-maximum energy distributions for IMFs 1–4 at select streamwise locations.

Since the integral in Eq. 12 is strictly positive, the peak energies are observed to increase monotonically when traversing downstream along the x axis. A comparison of the peak energy evolution for IMFs 1, 3, and 4 is presented in Fig. 34. From Fig. 34, the normalized growth rate between $x/x_0 = 3$ and $x/x_0 = 3.3$ is significantly more dominant in the case of IMF 3 in comparison with IMFs 1 and 4. As a consequence, the peak energy associated with IMF 3 grows to within 40% of saturation (> 60% of the corresponding maximum) by $x/x_0 \approx 3.35$. In contrast, the peak energies of IMFs 1 and 4 are observed at approximately 28% and 33% of the respective maxima, for the same streamwise position.

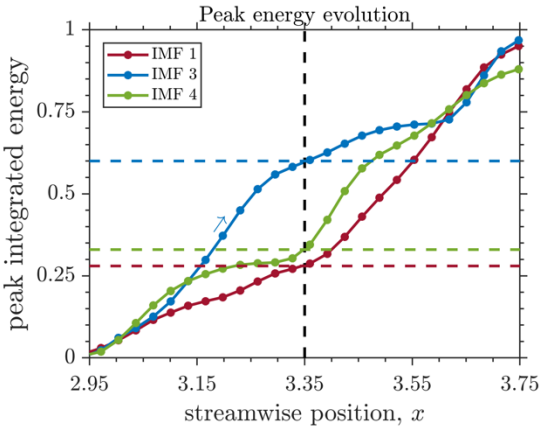

Fig. 34 Comparison of the peak energy evolution for IMFs 1, 3, and 4.

For reference, a comparison of the absolute peak energies for IMFs 1–4 is presented in Fig. 35, for select streamwise locations. The scatter points in Fig. 35 corresponding to a given streamwise

position have been displaced by a value of 10^{-10} with respect to the immediate upstream position, for clarity. From Fig. 35, the most energetic fluctuations between $x/x_0 = 3.1$ and $x/x_0 = 3.65$ are contained within IMF 4, spanning a range of wavenumbers between $\|k\| \approx 100$ and $\|k\| \approx 116$.

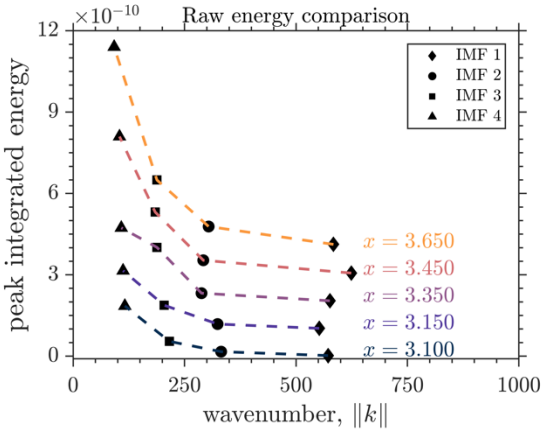

Fig. 35 Comparison of the absolute peak energies at select streamwise locations for IMFs 1–4.

The peak energy content across a unit length, referred to here as the peak energy density, was extracted for each IMF by projecting the corresponding gradient of peak E_I along the streamwise unit normal. The streamwise evolution of the peak energy densities for IMFs 1–4 is presented in Fig. 36 a). A dominant peak in the energy density evolution for IMF 4 appears around $x/x_0 = 3.4$, with an absolute value that is about an order of magnitude greater than the corresponding densities for IMFs 1–3 at the same streamwise location. The root mean square of the synthetic signal, $\emptyset_{rms}$, at any given point was calculated using a sliding kernel centered at that point and extending a distance of $\Delta x/x_0 = 0.025$ in the streamwise direction. The peak in the streamwise evolution of $\emptyset_{rms}$, presented in Fig. 36 b), appears at the same x-position as the peak in the local energy for IMF 4. Thus, the transverse velocity fluctuations are amplified in the near vicinity of $x/x_0 = 3.4$ resulting primarily from the large-wavelength oscillations of IMF 4 at $\|k\| \approx 104$. It is important to mention that this transient phase of intense fluctuations in the velocity is also accompanied with an increase in the skin friction and the Reynolds stress components, as described in the literature (Sayadi et al.,[1,41]). These transient overshoots appear prior to the establishment of a fully-developed turbulent boundary layer, which is observed beyond $x/x_0 = 3.7$ in the current transition process. Thus, the peak in the energy density for IMF 4 serves as a precursor to the end of the transition process and the appearance of a fully-developed turbulent boundary layer.

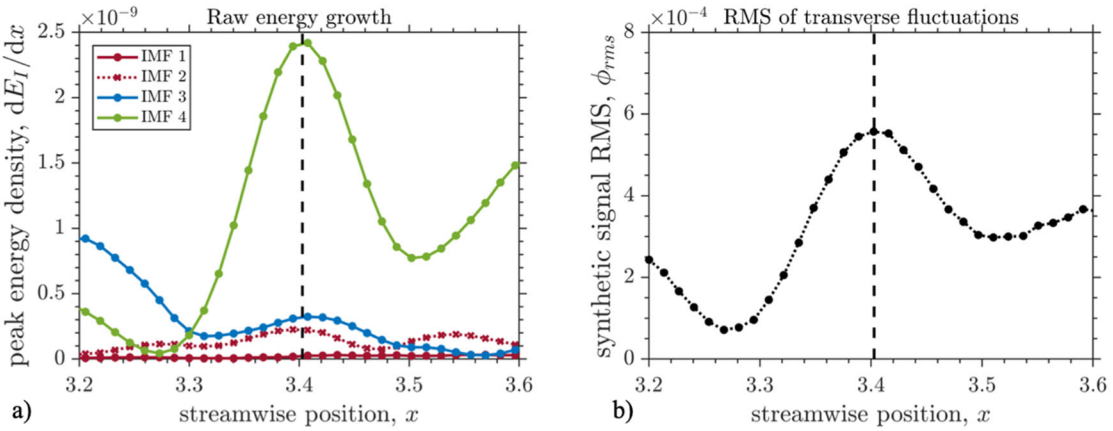

Fig. 36 a) Streamwise evolution of the peak energy densities for IMFs 1–4, b) RMS of the synthetic signal obtained using a sliding kernel with a streamwise spatial extent of $\Delta x = 0.025$.

Wavenumber Analysis across Nonlinear Breakdown

With the energy content associated with various modal component of the flow successfully identified from planar velocity fields, a more detailed survey into the flow spectral content was conducted. Given the physical importance of the oblique mode breakdown in the definition of the transitional flow process, it was also important to characterize the unsteady flow characteristics in the 3D velocity field across a range of spanwise wavenumbers. In order to provide this characterization, the *xz*-plane streamwise velocity fields were extracted from the flow domain and processed using the Riesz transform/log-Gabor filter analysis method described previously. The velocity field at select y/x_0 positions are shown in Fig. 37, where the velocity fluctuations due to the primary TS wave, the rapid growth of the secondary (oblique) instability, and the breakdown to a turbulent flow can be observed.

The approach used here allowed the variations in the spanwise wavenumber (k_z) spectra to be identified, corresponding to the excitation of the oblique instability and subsequent emergence of harmonics. This approach is in contrast to the earlier analysis in Fig. 32, where the spectra across the radially-averaged wavenumber was provided. However, given the physical implications of breakdown of this mode, it is of particular relevance to understanding the implications of the nonlinear breakdown process. The spanwise wavenumber spectra associated with the *u'* velocity fields shown in Fig. 37 were calculated, as shown in Fig. 38. These spectra were averaged across two periods of the primary TS wave to provide a generalized spectral representation of the energy within the transitional flow scales. The contour levels were also normalized for each spectrogram with the use of a moving average process in *x*, such that all wavenumbers at local streamwise regions can be clearly observed. Across *xz*-planes located at $y/x_0 \leq 0.005$, a narrow-band growth of the oblique mode can be observed across the region of $2 \leq x/x_0 \leq 2.5$. Downstream of this region, across $2.5 \leq x/x_0 \leq 3.2$, a rapid series of cascading bifurcations can be observed in the spectrograms through the emergence of numerous narrow-band harmonics of this fundamental mode. This harmonic excitation can be observed to be more rapid and energetic across the near-wall ($y/x_0 \leq 0.015$) region, as to compared to regions farther from the wall.

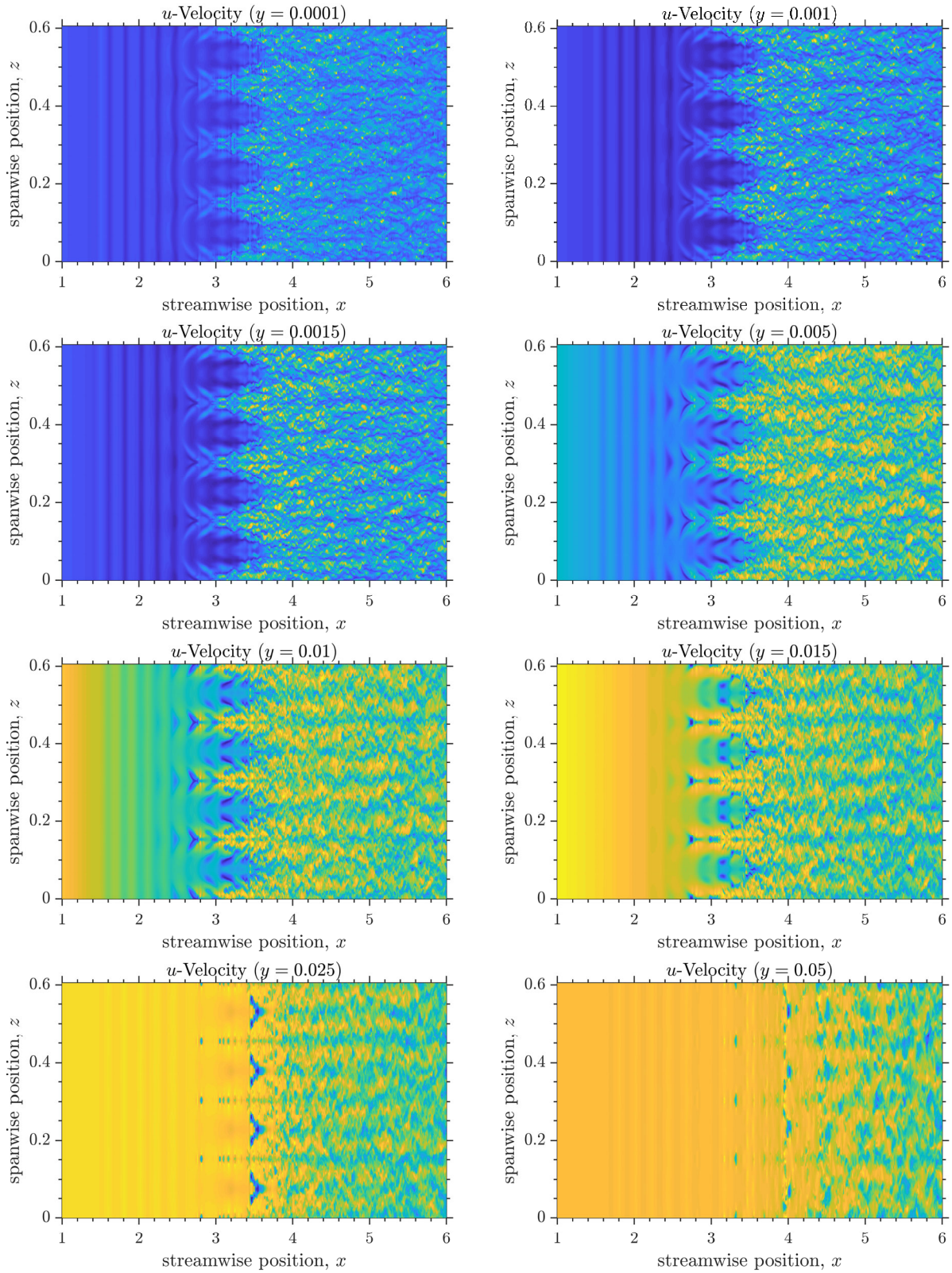

Fig. 37 Streamwise velocity field (instantaneous) across select *xz*-planes for spectrogram analysis.

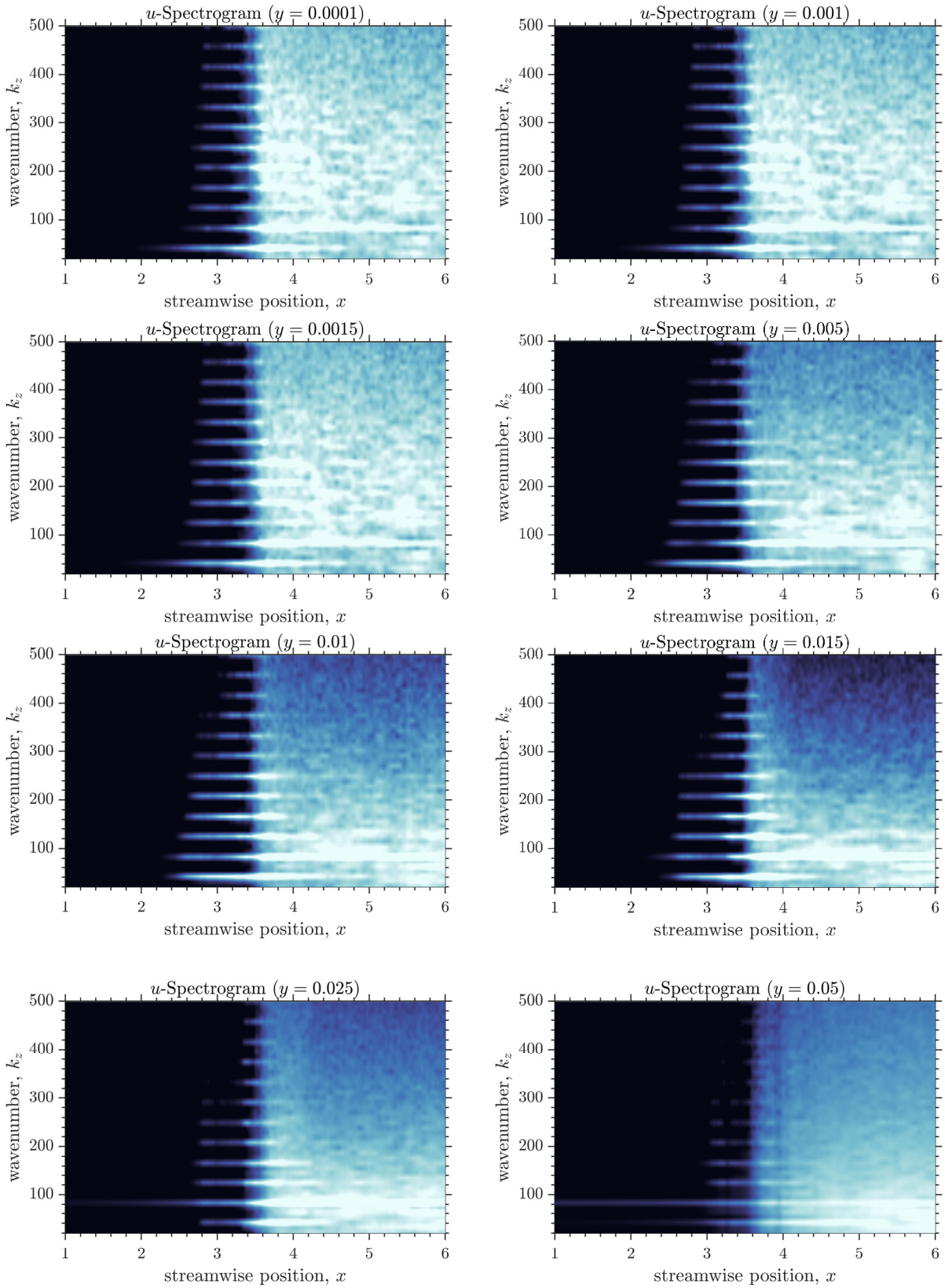

Fig. 38 Spectrogram of energy contained within spanwise fluctuation scales of *u'*, across transition process; averaged across two cycles of fundamental TS wave.

A physical comparison of Fig. 37 and Fig. 38 reveals that the growth of higher-wavenumber harmonics are produced initially by the emergence of increasingly-sharp edges in the Λ vortex structures, and the emergence of progressively smaller flow fluctuation scales, by definition. In this way, characterizing the spectral content of a sharp-edged corner in Fourier space can be anticipated to produce a spectrum with these features. However, the aforementioned region of harmonic excitation, $2.5 \leq x/x_0 \leq 3.2$, is also observed in Fig. 37 to conclude with the initiation of classically-described turbulent spots. With further streamwise distance, to $x/x_0 = 3.5$, the wavenumber spectrograms in Fig. 38 corresponding to $y/x_0 \leq 0.015$ are all observed to reveal a nearly-discontinuous, sudden emergence of a broad-band energy content covering a classically-defined turbulent spectrum. In the u velocity fields of Fig. 37, this position corresponds to the instance where the spanwise-periodic turbulent wedges merge, resulting in a full spanwise coverage of turbulent boundary layer behavior. It is of particular interest that the entire spectrum of turbulent scales emerge so rapidly, as the broad-band behavior does not appear to be linked directly to any oblique mode wavenumber scale. However, another interesting observation is the persistence of several narrow-band peaks in these spectrograms beyond the emergence of the broad-band turbulent flow characteristics. This persistence further suggests that a dispersion of the initial transitional flow scales are not fundamental characteristics of sustaining the early turbulent flow, but rather it is more likely that the energy content within these flow scales are gradually mixed through an energy cascade process towards an isotropic behavior far downstream.

From Fig. 38, it can also be subtly observed that the streamwise position where the broad-band wavenumber energy distribution is initiated occurs farther downstream as the y position is increased to higher regions of the boundary layer. This characteristic is further exemplified in Fig. 39, where the wavenumber-integrated power of the spectrograms are shown for various y positions as a function of streamwise position. Unlike the spectrograms in Fig. 38, the amplitude of the averaged power was not renormalized based on a moving average in x. Similar to previous observations, a rapid growth of the mean power can be observed for regions with $y/x_0 \leq 0.015$, until a maximum power is reached at a streamwise position of $x/x_0 = 3.5$. Across regions of the boundary layer farther from the wall, a decrease in the overall power values within the spectra are observed, alongside a downstream shift of the position where the maximum power value is encountered.

These observations are further typified by the magnitude of the streamwise velocity fluctuations (u'_{rms}) as shown in Fig. 40. Here, the rapid increase in turbulent fluctuations can be observed, initiating at $x/x_0 = 3.5$ and $y/x_0 \leq 0.025$, and subsequently progressing into regions farther away from the wall with increased streamwise distance. Incidentally, the streamwise region where this large increase in unsteadiness is also that associated with the observed overshoot in skin friction in the transitional boundary layer, as shown in Fig. 41 after Sayadi et al.[1] In this way, an increase in $C_{f,x}$ is observed in the late stages of transition, featuring a maximum value that exceeds the classical turbulent correlation value for skin friction. For the current dataset, an increase in $C_{f,x}$ beyond the conventional turbulent correlation is observed from $3.5 \leq x/x_0 \leq 4$, at which point a peak in skin friction is observed. Downstream of this position, the degree of

overshoot observed in the skin friction coefficient gradually decreases, until a value approximately coincident with the turbulent correlation is reached at x/x_0 = 6.0. With the presence of *both* the broad-band turbulent flow spectral content, as well as the persistence of the flow scales associated with the oblique mode, it is postulated that the source of this skin friction overshoot is linked to the contribution of the former component within the wavenumber spectrum. The continued presence of narrow-band peaks in the spectrograms of Fig. 38 and gradual subsiding as x/x_0 = 6.0 is reached, provides conceptual support of this conjecture.

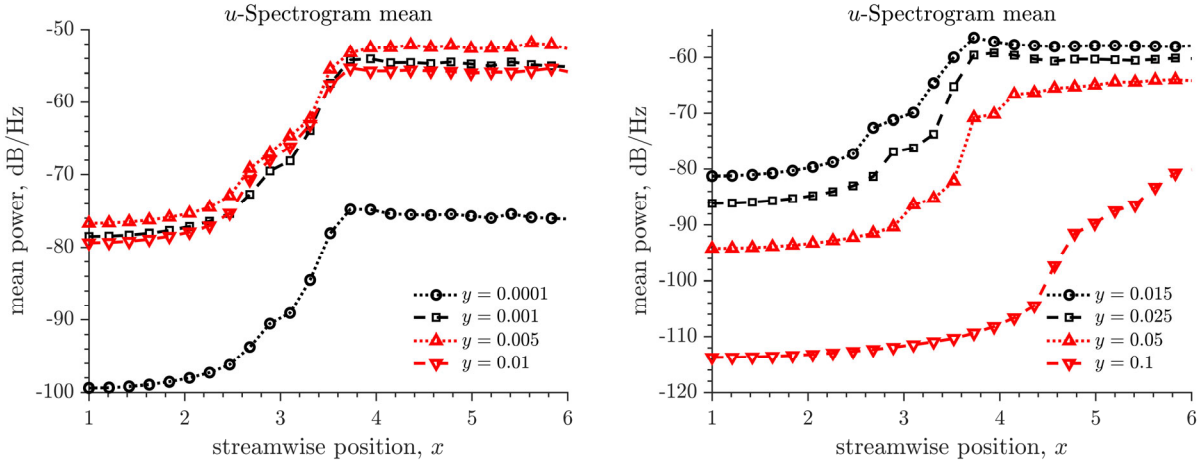

Fig. 39 Averaged power, integrated across spectrum, of spanwise fluctuations in *u'* across transition process.

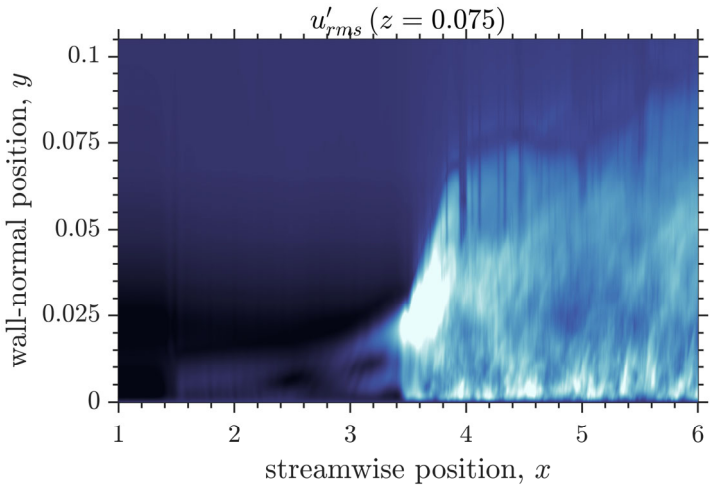

Fig. 40 Magnitude of streamwise velocity fluctuations (u'_{rms}) localized to center of *Λ* vortex, demonstrating peak in unsteadiness coincident with emergence of broad-band behavior in spectrograms.

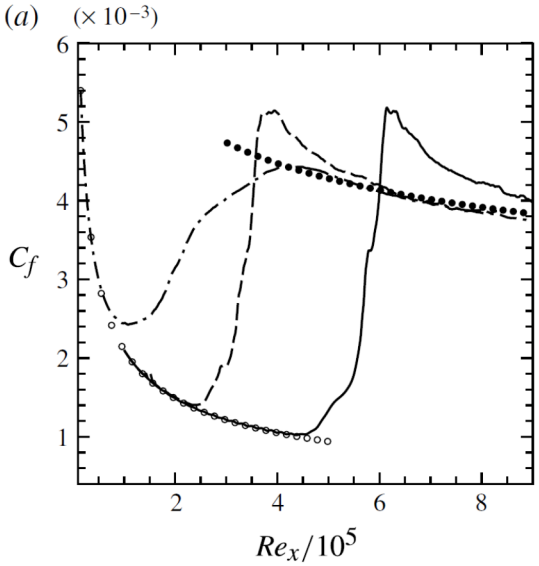

Fig. 41 Variation in skin friction coefficient with Re_x for transitional boundary layer: K-type transition process shown by dashed curve, with Blasius solution as open circles and turbulent correlation as closed circles, after Sayadi et al.[1]

Conclusions

The results of the current study provide several important developments in the processing and analysis of complex, volumetric flow fields. The ability to perform adaptive decomposition based on relative flow scale rather than projection to a fixed basis lifts several limitations of incumbent alternative methods of studying fluid flows. Additionally, coupling these scale-based decomposition methods with the filtered-Riesz transform allows an analog to a 3D Hilbert analysis to be conducted. In this way, the localized evolution of energy within specific components of a wavenumber spectrum can be performed. This approach provides a powerful avenue to understand the development of wave behaviors in fluid flows generally, though it has found a compelling case study in the application to transitional flow physics.

Experimental data acquired for a 2D controlled transition process revealed the presence of large-scale coherent vortex structures consistent with historical observations of hairpin and *Λ*-shaped vortices. Through a POD reconstruction process, the large-scale features were observed to be the predominant contributor to the overshoots observed in the skin friction coefficient across the transitional boundary layer, consistent with other observations in the literature.

The application of EMD to DNS data for a K-type boundary-layer transition process identified morphological evidence of flow structures emerging with decreasing length scale throughout the nonlinear breakdown phase of transition. The presence of these scales were also identified in a 3D Fourier analysis of the IMFs obtained from the EMD processing. Interestingly, the presence of the wavenumber characteristic of the primary TS wave were observed downstream of the streamwise position where the boundary layer had completed the transition process. This observation was further corroborated by a localized study of the wavenumber spectra, which further revealed the importance of large-scale structures in the transition process and cumulative

energy of the flow. Further characterization of spectrograms within the velocity field revealed a rapid emergence of harmonics of the oblique mode, consistent with early studies on harmonic excitation in the transition process. However, the truly rapid, cascading nature of these harmonics can be more significantly appreciated with the ability to directly observe the evolutionary characteristics via the spectrograms.

By inspection of the evolution of the spectral content, the appearance of a broad-band region of energetic wavenumbers was abruptly introduced, coincident with the flow region where the localized turbulent spots merged, forming a turbulent flow covering the entire spanwise domain of the flow. The sudden appearance of this broad-band content suggests that the physical scales of the TS wave or oblique mode have little influence on directly dictating the initial characteristics of the broad-band component of the turbulent flow spectrum. While breakdown of the oblique mode is a physical mechanism that triggers the emergence of the broad-band flow scales, it does not appear to directly influence the canonical turbulence spectrum in any perceptible way after the turbulent spots have merged. However, the presence of narrow-band peaks associated with the oblique mode and several harmonics are observed to persist after the completion of the transition process. The flow also appears to have a dramatic increase in unsteadiness localized to the streamwise position where the boundary-layer flow is assumed to be entirely turbulent across the entire spanwise domain, which occurs farther upstream across regions closer to the wall, with this high-energy region moving farther away from the wall with increasing streamwise distance. The retention of the narrow-band spectral content associated with large-scale oblique mode structures is conjectured to be a significant contributor to the overshoot mechanism observed in the skin friction coefficient during the natural transition process. As the signature of these large-scale features begin to dissipate in the spectrograms, the skin friction coefficient appears to converge to the typical correlation value for a turbulent boundary layer.

References

[1] Sayadi, T., Hamman, C., and Moin, P., "Direct numerical simulation of complete H-type and K-type transitions with implications for the dynamics of turbulent boundary layers," *Journal of Fluid Mechanics*, Vol. 724, 2013, pp. 480-509. doi:10.1017/jfm.2013.142

[2] Blois, G., Christensen, J., Bests, J., Elliott, G., Austin, J., Dutton, J.C., Bragg, M., Garcia, M., and Fouke, B., "A versatile refractive-index-matched flow facility for studies of complex flow systems across scientific disciplines," AIAA Paper 2012-0736, 2012.

[3] K. Bai and J. Katz, "On the refractive index of sodium iodide solutions for index matching in PIV," Exp. Fluids 55, 1704 (2014).

[4] A. M. Hamed, A. Kamdar, L. Castillo, and L. P. Chamorro, "Turbulent boundary layer over 2D and 3D large-scale wavy walls," Phys. Fluids 27, 106601 (2015).

[5] G. B. Schubauer and H. K. Skramstad, "Laminar boundary-layer oscillations and transition on a flat plate," J. Res. Natl. Bur. Stand. 38, 92 (1947).

[6] A. V. Boiko, K. J. A. Westin, B. G. B. Klingmann, V. V. Kozlov, and P. H. Alfredsson, "Experiments in a boundary layer subjected to free stream turbulence. Part 2. The role of TS-waves in the transition process," J. Fluid Mech. 281, 219–245 (1994).

[7] V. Gilev and V. Kozlov, “Excitation of Tollmien–Schlichting waves in a boundary layer on a vibrating surface,” Zh. Prikl. Mekh. Tekh. Fiz. 1, 73–77 (1984).
[8] P. S. Klebanoff, K. D. Tidstrom, and L. M. Sargent, “The three-dimensional nature of boundary-layer instability,” J. Fluid Mech. 12, 1–34 (1962).
[9] H. Schlichting, “Zur enstehung der turbulenz bei der plattenstr€omung,” Nachr. Ges. Wiss. Goettingen, Math.-Phys. Kl. 1933, 181–208; available at http://eudml.org/doc/59420
[10] W. Tollmien, “General instability criterion of laminar velocity distributions,” National Advisory Committee for Aeronautics (NACA) Technical Memorandum No. NACA-TM-792, 1936.
[11] P. G. Drazin, Introduction to Hydrodynamic Stability (Cambridge University Press, 2002), Vol. 32.
[12] P. G. Drazin and W. H. Reid, Hydrodynamic Stability (Cambridge University Press, 2004).
[13] S. Wu, K. T. Christensen, and C. Pantano, “A study of wall shear stress in turbulent channel flow with hemispherical roughness,” J. Fluid Mech. 885, A16 (2020).
[14] M. S. Acarlar and C. R. Smith, “A study of hairpin vortices in a laminar boundary layer. Part 1. Hairpin vortices generated by a hemisphere protuberance,” J. Fluid Mech. 175, 1–41 (1987).
[15] K. Taira, S. L. Brunton, and S. T. M. Dawson, “Modal analysis of fluid flows: An overview,” AIAA J. 55, 4013–4041 (2017).
[16] D. Rempfer and H. F. Fasel, “Evolution of three-dimensional coherent structures in a flat-plate boundary layer,” J. Fluid Mech. 260, 351–375 (1994).
[17] G. Berkooz, P. Holmes, and J. L. Lumley, “The proper orthogonal decomposition in the analysis of turbulent flows,” Annu. Rev. Fluid Mech. 25, 539–575 (1993).
[18] P. Holmes, J. L. Lumley, G. Berkooz, and C. W. Rowley, Turbulence, Coherent Structures, Dynamical Systems and Symmetry (Cambridge University Press, 2012).
[19] L. Sirovich, “Turbulence and the dynamics of coherent structures. i. Coherent structures,” Q. Appl. Math. 45, 561–571 (1987).
[20] C. Vanderwel, A. Stroh, J. Kriegseis, B. Frohnapfel, and B. Ganapathisubramani, “The instantaneous structure of secondary flows in turbulent boundary layers,” J. Fluid Mech. 862, 845–870 (2019).
[21] A.M.Hamed,M. J. Sadowski,H. M. Nepf, and L. P. Chamorro, “Impact of height heterogeneity on canopy turbulence,” J. Fluid Mech. 813, 1176–1196 (2017).
[22] K. E. Meyer, J. M. Pedersen, and O. €Ozcan, “A turbulent jet in crossflow analysed with proper orthogonal decomposition,” J. Fluid Mech. 583, 199–227 (2007).
[23] Huang, N.E., Shen, Z., Long, S.R., Wu, M.C., Shih, H.H., Zheng, Q., Yen, N., Tung, C.C., and Liu, H.H., “The Empirical Mode Decomposition and the Hilbert Spectrum for Nonlinear and Non-Stationary Time Series Analysis,” *Proceedings of the Royal Society London A*, Vol. 454, 1998, pp. 903-995.
[24] S.M. Bhuiyan, R. R. Adhami, and J. F. Khan, “Fast and adaptive bidimensional empirical mode decomposition using order-statistics filter based envelope estimation,” *EURASIP J. Adv. Signal Process*., vol. 2008, no. 1,
2008, Art. no. 728356.
[25] C.-Y. Chen, S.-M. Guo, W.-S. Chang, J. S.-H. Tsai, and K.-S. Cheng, “An improved bidimensional empirical mode decomposition: A mean approach for fast decomposition,” *Signal Process*., vol. 98, pp. 344–358,
2014.

[26] J. C. Nunes, Y. Bouaoune, E. Delechelle, O. Niang, and P. Bunel, “Image analysis by bidimensional empirical mode decomposition,” *Image Vis. Comput*., vol. 21, no. 12, pp. 1019–1026, 2003.
[27] J. C. Nunes, O. Niang, Y. Bouaoune, E. Delechelle, and P. Bunel, “Texture analysis based on the bidimensional empirical mode decomposition with gray-level co-occurrence models,” in *Proc. 7th Int. Symp. Signal Process*. *Appl*., 2003, vol. 2, pp. 633–635.
[28] J. Riffi, A. M. Mahraz, A. Abbad, and H. Tairi, “3D extension of the fast and adaptive bidimensional empirical mode decomposition,” *Multidimensional Syst. Signal Process.*, vol. 26, no. 3, pp. 823–834, 2015.
[29] A. Ahrabian, N. ur Rehman, and D. P.Mandic, “Bivariate empirical mode decomposition for unbalanced real-world signals,” *IEEE Signal Process. Lett.*, vol. 20, no. 3, pp. 245–248, Mar. 2013.
[30] A. Hemakom, V. Goverdovsky, D. Looney, and D. P. Mandic, “Adaptive projection intrinsically transformed multivariate empirical mode decomposition in cooperative brain–computer interface applications,” *Philos. Trans. Roy. Soc. A*, vol. 374, no. 2065, 2016, Art. no. 20150199
[31] D. Looney, A. Hemakom, and D. P. Mandic, “Intrinsic multi-scale analysis: A multi-variate empirical mode decomposition framework,” *Proc. Roy. Soc. A*, vol. 471, no. 2173, 2015, Art. no. 20140709.
[32] D. P. Mandic, N. ur Rehman, Z. Wu, and N. E. Huang, “Empirical mode decomposition-based time-frequency analysis of multivariate signals: The power of adaptive data analysis,” *IEEE Signal Process.Mag.*, vol. 30, no. 6, pp. 74–86, Nov. 2013.
[33] N. Rehman and D. P. Mandic, “Multivariate empirical mode decomposition,” *Proc. Roy. Soc. London A, Math., Phys. Eng. Sci.*, 2009.
[34] N. ur Rehman, C. Park, N. E. Huang, and D. P.Mandic, “EMD via MEMD: Multivariate noise-aided computation of standard EMD,” *Adv. Adaptive Data Anal.*, vol. 5, no. 2, 2013, Art. no. 1350007.
[35] N. ur Rehman, M. W. Safdar, U. ur Rehman, and D. P. Mandic, “Dynamically-sampled bivariate empirical mode decomposition,” *IEEE*
Signal Process. Lett., vol. 21, no. 7, pp. 857–861, Jul. 2014.
[36] Z. Wu, N. E. Huang, and X. Chen, “The multi-dimensional ensemble empirical mode decomposition method,” *Adv. Adaptive Data Anal.*, vol. 1, no. 3, pp. 339–372, 2009.
[37] Z. He, J. Li, L. Liu, and Y. Shen, “Three-dimensional empirical mode decomposition (TEMD): A fast approach motivated by separable filters,” *Signal Process.*, vol. 131, pp. 307–319, 2017.
[38] Gabor, D., “Theory of Communication, Part 1: The Analysis of Information,” *Journal of the Institution of Electrical Engineers-Part III: Radio and Communication Engineering*, Vol. 93, No. 26, 1946, pp. 429–441.
doi: 10.1049/ji-3-2.1946.0074
[39] Vakman, D., “On the Definition of Concepts of Amplitude, Phase and Instantaneous Frequency of a Signal,” *Radio Engineering and Electronic Physics*, Vol. 17, No. 5, 1972, pp. 754–759.
[40] Felsberg, M., and Sommer, G., “The Monogenic Signal,” *IEEE Transactions on Signal Processing*, Vol. 49, No. 12, 2001, pp. 3136–3144.
doi: 10.1109/78.969520

[41] T. Sayadi, J. Nichols, P. Schmid, and M. Jovanovic, “Dynamic mode decomposition of H-type transition to turbulence,” in Proceedings of the Summer Program (Citeseer, 2012), p. 5.
[42] A. Lozano-Dur_an, M. Hack, and P. Moin, “Modeling boundary-layer transition in direct and large-eddy simulations using parabolized stability equations,” Phys. Rev. Fluids 3, 023901 (2018).
[43] S. Sharma, M. S. Shadloo, and A. Hadjadj, “Laminar-to-turbulent transition in supersonic boundary layer: Effects of initial perturbation and wall heat transfer,” Numer. Heat Transfer, Part A 73, 583–603 (2018).
[44] T. P. Wadhams, E. Mundy, M. G. MacLean, and M. S. Holden, “Ground test studies of the HIFiRE-1 transition experiment part 1: Experimental results,” J. Spacecr. Rockets 45, 1134–1148 (2008).
[45] R. J. Adrian, “Hairpin vortex organization in wall turbulence,” Phys. Fluids 19, 041301 (2007).
[46] J. Zhou, R. J. Adrian, S. Balachandar, and T. M. Kendall, “Mechanisms for generating coherent packets of hairpin vortices in channel flow,” J. Fluid Mech. 387, 353–396 (1999).
[47] T. Theodorsen, “Mechanisms of turbulence,” in Proceedings of the 2nd Midwestern Conference on Fluid Mechanics (1952), p. 1952.
[48] T. Theodorsen, “The structure of turbulence,” in 50 Jahre Grenzschichtforschung (Springer, 1955), pp. 55–62.
[49] J. Jeong, F. Hussain, W. Schoppa, and J. Kim, “Coherent structures near the wall in a turbulent channel flow,” J. Fluid Mech. 332, 185–214 (1997).
[50] R. J. Adrian, C. D. Meinhart, and C. D. Tomkins, “Vortex organization in the outer region of the turbulent boundary layer,” J. Fluid Mech. 422, 1–54 (2000).
[51] D. J. C. Dennis, “Coherent structures in wall-bounded turbulence,” An. Acad. Bras. Cienc. 87, 1161–1193 (2015).
[52] K. T. Christensen and R. J. Adrian, “Statistical evidence of hairpin vortex packets in wall turbulence,” J. Fluid Mech. 431, 433–443 (2001).
[53] W. T. Hambleton, N. Hutchins, and I. Marusic, “Simultaneous orthogonal plane particle image velocimetry measurements in a turbulent boundary layer,” J. Fluid Mech. 560, 53–64 (2006).
[54] H. Wang, G. Peng, M. Chen, and J. Fan, “Analysis of the interconnections between classic vortex models of coherent structures based on DNS data,” Water 11, 2005 (2019).
[55] Moin, P., Leonard, A. and Kim, J., “Evolution of a curved vortex filament into a vortex ring,” *The Physics of fluids*, Vol. 29, No. 4, 1986, pp. 955-963.
[56] Bake, S., Meyer, D.G.W. and Rist, U., ”Turbulence mechanism in Klebanoff transition: a quantitative comparison of experiment and direct numerical simulation,” *Journal of Fluid Mechanics*, Vol. 459, 2002 pp.217-243.
[57] Hambleton, W.T., Hutchins, N. and Marusic, I., “Simultaneous orthogonal-plane particle image velocimetry measurements in a turbulent boundary layer,” *Journal of Fluid Mechanics*, Vol. 560, 2006, pp.53-64.
[58] Bridge, C.P., 2017. Introduction to the monogenic signal. *arXiv preprint arXiv:1703.09199*.